Received: 7 April 2023 | Revised: 30 August 2023 | Accepted: 7 September 2023

DOI: 10.1002/cac2.12486

CANCER COMMUNICATIONS Open Access

ORIGINAL ARTICLE

Interactions of Indoleamine 2,3-dioxygenase-expressing LAMP3$^+$ dendritic cells with CD4$^+$ regulatory T cells and CD8$^+$ exhausted T cells: synergistically remodeling of the immunosuppressive microenvironment in cervical cancer and therapeutic implications

Xinyu Qu[1,2] | **Yumeng Wang**[1,2] | **Qian Jiang**[1,2] | **Tingting Ren**[1,2] | **Chenyan Guo**[1,2] | **Keqin Hua**[1,2] | **Junjun Qiu**[1,2]

[1]Department of Gynecology, Obstetrics and Gynecology Hospital, Fudan University, Shanghai, P. R. China

[2]Shanghai Key Laboratory of Female Reproductive Endocrine-Related Diseases, Shanghai, P. R. China

Correspondence
Junjun Qiu, Keqin Hua and Chenyan Guo, Department of Gynecology, Obstetrics and Gynecology Hospital, Fudan University, 419 Fangxie Road, Shanghai 200011, P. R. China.
Email: qiujunjun1113@163.com, huakeqin@fudan.edu.cn and guochenyan357901@163.com

Funding information
Shanghai Science and Technology, Grant/Award Numbers: 21Y11906900, 22Y3190050; Shanghai Hospital Development Center, Grant/Award Numbers: SHDC2020CR1045B, SHDC2020CR6009, SHDC2020CR4087, SHDC22021307; Shanghai Municipal Health Commission, Grant/Award Number: 202040498; National Natural Science Foundation of China,

Abstract

Background: Cervical cancer (CC) is the fourth most common cancer in women worldwide. Although immunotherapy has been applied in clinical practice, its therapeutic efficacy remains far from satisfactory, necessitating further investigation of the mechanism of CC immune remodeling and exploration of novel treatment targets. This study aimed to investigate the mechanism of CC immune remodeling and explore potential therapeutic targets.

Methods: We conducted single-cell RNA sequencing on a total of 17 clinical specimens, including normal cervical tissues, high-grade squamous intraepithelial lesions, and CC tissues. To validate our findings, we conducted multicolor immunohistochemical staining of CC tissues and constructed a subcutaneous tumorigenesis model in C57BL/6 mice using murine CC cell lines (TC1) to evaluate the effectiveness of combination therapy involving indoleamine 2,3-dioxygenase 1 (IDO1) inhibition and immune checkpoint blockade (ICB). We used the unpaired two-tailed Student's t-test, Mann-Whitney test, or Kruskal-Wallis test to compare continuous data between two groups and one-way ANOVA with Tukey's post hoc test to compare data between multiple groups.

Abbreviations: ADC, adenocarcinoma; AHR, aryl hydrocarbon receptor; APC, antigen-presenting cell; CC, cervical cancer; CESC, cervical and endocervical cancer; CNV, copy number variation; DC, dendritic cell; E, epacadostat; HPV, human papillomavirus; HSIL, high-grade squamous intraepithelial lesion; ICB, immune checkpoint blockade; IHC, immunohistochemistry; Kyn, kynurenine; MHC, major histocompatibility complex; Ex, exhausted; Nex, non-exhausted; Nre, non-reactive to tumor antigen; ORR, objective response rate; Re, reactive to tumor antigen; SCC, squamous cell carcinoma; scRNA-seq, single-cell RNA sequencing; SD, standard deviation; TCGA, The Cancer Genome Atlas; TCR, T cell receptor; TIL, tumor-infiltrating lymphocyte; TIME, tumor immune microenvironment; TLR, toll-like receptor; TME, tumor microenvironment.

Xinyu Qu, Yumeng Wang and Qian Jiang has contributed equally to this work.

Grant/Award Numbers: 81971361, 82173188; Fudan University, Grant/Award Number: JIF157600

Results: Malignant cervical epithelial cells did not manifest noticeable signs of tumor escape, whereas lysosomal-associated membrane protein 3-positive ($LAMP3^+$) dendritic cells (DCs) in a mature state with immunoregulatory roles were found to express IDO1 and affect tryptophan metabolism. These cells interacted with both tumor-reactive exhausted $CD8^+$ T cells and $CD4^+$ regulatory T cells, synergistically forming a vicious immunosuppressive cycle and mediating CC immune escape. Further validation through multicolor immunohistochemical staining showed co-localization of neoantigen-reactive T cells ($CD3^+$, $CD4^+$/$CD8^+$, and PD-1^+) and $LAMP3^+$ DCs ($CD80^+$ and PD-$L1^+$). Additionally, a combination of the IDO1 inhibitor with an ICB agent significantly reduced tumor volume in the mouse model of CC compared with an ICB agent alone.

Conclusions: Our study suggested that a combination treatment consisting of targeting IDO1 and ICB agent could improve the therapeutic efficacy of current CC immunotherapies. Additionally, our results provided crucial insights for designing drugs and conducting future clinical trials for CC.

KEYWORDS

cervical cancer, dendritic cell, immune checkpoint blockade, immune escape, indoleamine 2,3-dioxygenase 1, single-cell analysis, T cell

1 | BACKGROUND

Cervical cancer (CC) is the fourth most common cancer in women worldwide, with approximately 85% of cases occurring in developing countries [1]. Surgery, radiotherapy, and chemotherapy are the main treatments for CC. Immunotherapy has become a novel treatment option for patients with recurrent metastatic disease. In the past decade, multiple clinical trials [2–5] have been conducted to investigate the efficacy of immune checkpoint blockade (ICB) agents, such as pembrolizumab (anti-PD-1 antibody), nivolumab (anti-PD-1 antibody), and zalifrelimab (anti-CTLA4 antibody), in patients with recurrent or metastatic CC. Although pembrolizumab was approved by the U.S. Food and Drug Administration based on the KEYNOTE-158 trial (NCT2628067), the objective response rate of currently developed ICB drugs seldom reaches 30%, and their administration is sometimes accompanied by serious treatment-related adverse events. Immunotherapy for CC has tremendous room for improvement in efficacy.

To further enhance the efficacy of immunotherapy, the mechanism of tumor immune microenvironment (TIME) remodeling needs to be understood. Based on the concept of cancer immune editing [6], cancer development comprises of 3 "E" phases: elimination, equilibrium, and escape. Elimination is the process by which the immune system recognizes and eradicates cancer cells. Equilibrium is a state of tumor latency during which tumor cells remain subclinical, in which tumor cells are not completely removed yet do not increase in number. Escape is the phase in which tumor cells are capable of evading immune recognition and elimination, leading to unlimited tumor growth and progression. In general, tumor immune evasion and an immunosuppressive microenvironment lead to inefficient tumor eradication. Previous studies of CC on immune escape and suppression have either focused on well-known immune checkpoint inhibitors, such as PD-L1 [7], offering little novel value or merely reported phenotypic changes in certain immune cell types [8], failing to present a convincing molecular mechanism. Considering that the mechanisms underlying CC escape and immune microenvironment remodeling remain elusive, further investigations are needed for achieving immunotherapy with high efficacy.

Using single-cell RNA sequencing (scRNA-seq), intratumoral transcriptional heterogeneity, and cellular crosstalk within the tumor microenvironment (TME) have been extensively studied in various cancers [9–11]. Notably, the latest studies on lung and gastrointestinal cancers [12, 13] demonstrated that scRNA-seq could be utilized to characterize tumor-infiltrating lymphocytes (TILs) that are specifically reactive towards tumor-associated neoantigens, which were reported to be key elements for determining treatment efficacy in each patient. Thus, using

the powerful scRNA-seq tool, concentrating on unique cell subpopulations and associated cellular interactions that mediate immune suppression within the CC TME might offer insights on improving the therapeutic effects of immunotherapy for CC.

In the present study, we aimed to identify specific cellular interactions and elucidate the potential mechanisms mediating CC immune escape. A comprehensive investigation through scRNA-seq was conducted on not only malignant cervical epithelial cells but also immune populations, including dendritic cells (DCs) and T cells. With experimental validation, our study pioneeringly provided novel insights into how to further improve the efficacy of current immunotherapies for CC.

2 | MATERIALS AND METHODS

2.1 | Human specimens

A total of 3 formalin-fixed, paraffin-embedded CC samples along with 2 normal cervix samples and 2 high-grade squamous intraepithelial lesions (HSIL) tissues for multicolor immunohistochemistry (IHC) staining were collected from the tissue bank of the Obstetrics and Gynecology Hospital of Fudan University, Shanghai, China, under the approval of Ethics Committee (2020-22) with informed consent. CC samples were obtained during primary treatment of surgical resection while normal cervix and HSIL tissues were obtained during colposcopy biopsies with pathologic diagnosis by two qualified pathologists. More detailed clinicopathological information of these 7 samples were listed in Supplementary Table S1.

2.2 | Cell lines

The TC-1 cell line was purchased from the Chinese Academy of Sciences Shanghai Cellular Library (Shanghai, China). Cells were maintained in RPMI 1640 medium (Gibco, Gaithersburg, MD, USA) supplemented with 100 IU/mL penicillin G (Sangon Biotec, Shanghai, China), 100 mg/mL streptomycin sulfate (Sangon Biotech), and 10% FBS (Gibco) under a humidified atmosphere of 5% CO_2 at 37°C.

2.3 | scRNA-seq datasets

To acquire transcriptomic profiles during the malignant transition of the cervix, we obtained 10x Genomics scRNA-seq data from 17 cervical tissue samples that were previously generated by our group (Gene Expression Omnibus accession number: GSE197461 [14] and GSE208653 [15]. GSE197461 dataset consisting of both scRNA-seq and T cell receptor-sequencing [TCR-seq data] and GSE208653 dataset consisting of scRNA-seq data) altogether included 4 normal cervical tissue samples, 2 HSIL samples obtained by colposcopy biopsy and 11 CC tissues (5 squamous cell carcinoma [SCC] samples and 6 adenocarcinoma [ADC] samples) by surgical resection with pathological diagnosis. All 11 patients with CC were primarily treated preoperatively at FIGO stages I-II. The exclusion criteria were as follows: (1) serious concomitant systemic disorder, (2) history of chemotherapy or radiotherapy, (3) history of malignant tumors other than CC, and (4) evidence of distant metastasis. The detailed clinical characteristics of the 17 CC samples are presented in Supplementary Table S1.

2.4 | scRNA-seq data processing and analysis

scRNA-seq data were analyzed using the NovelBrain Cloud Analysis Platform (www.novelbrain.com). We applied fastp [16] with default parameters to filter the adaptor sequences and remove low-quality reads to obtain clean data. Subsequently, feature-barcode matrices were obtained by aligning the reads to the human genome (GRCh38 Ensemble, version 100) using CellRanger (version 5.0.1, 10x Genomics). We applied Downsampling analysis to the samples that were sequenced according to the mapped barcoded reads per cell of each sample to ultimately achieve the aggregated matrix. Cells containing over 200 expressed genes and a mitochondrial unique molecular identifier (UMI) rate below 20% were subjected to cell quality filtering, and mitochondrial genes were removed from the expression table.

The Seurat package (version 3.1.4; https://satijalab.org/seurat/) was used for cell normalization and regression based on the expression table according to the UMI counts of each sample and the percentage of mitochondrial genes to obtain the scaled data. The fastMNN function (k = 5, d = 50, approximate = TRUE) in the R package scan (v1.12.1) was used for applying the mutual nearest-neighbor method to correct for batch effects among samples. Using a graph-based cluster method, we acquired unsupervised cell cluster results based on the top 10 principal components in principal component analysis (PCA) and calculated the marker genes using the FindAllMarkers function with the Wilcoxon rank-sum test algorithm under the following criteria: Ln[fold change, (FC)> 0.25, P value < 0.05, and min.pct (minimum percentage) > 0.1. To identify the cell types in detail, clusters of the same cell type were selected for another round of uniform manifold approximation and projection (UMAP), graph-based clustering, and marker analysis.

2.5 | Copy number variation (CNV) estimation

In scRNA-seq analysis, endothelial cells, fibroblasts and smooth muscle cells were used as references to identify somatic CNVs using the R package inferCNV (version 0.8.2). Each cell was scored according to the extent of the CNV signal, defined as the mean of the squared CNV values across the genome. Putative malignant cells were defined as those with a CNV signal > 0.04 and CNV correlation > 0.5.

2.6 | Differential gene expression analysis

In scRNA-seq analysis, to identify differentially expressed genes among the groups (malignant epithelial cells *vs.* non-malignant epithelial cells), the FindMarkers function with the Wilcoxon rank sum test algorithm was used. Significantly differentially expressed genes were selected as those that met the following criteria: (1) lnFC > 0.25, (2) *P* value < 0.05, and (3) min.pct > 0.1.

2.7 | Pseudotime analysis

Single-cell trajectory analysis was performed using Monocle2 [17] (http://cole-trapnell-lab.github.io/monocle-release) with DDR-Tree and default parameters to determine the dramatic translational relationships among cell types and clusters. Before Monocle2 analysis, we selected marker genes from the Seurat clustering results and raw expression counts from the cells that passed the filtering.

2.8 | QuSAGE analysis

To characterize the relative activation of a given gene set, such as KEGG and metabolic gene sets, we performed QuSAGE (2.16.1) analysis [18]. Briefly, Briefly, QuSAGE accounted for inter-gene correlations and corrected these correlations by improving the estimation of the variance inflation factor from expression data.

2.9 | Cellular interaction analysis

We conducted cellular interaction analysis using CellPhoneDB (https://www.cellphonedb.org) [19], a public repository of ligands, receptors, and their interactions; this enables a systematic analysis of cell-cell communication at the molecular level. Membranous, secreted, and peripheral proteins were annotated. The significant mean and cell communication significance ($P < 0.05$) were calculated on the basis of the interactions and normalized cell matrix achieved by Seurat normalization.

2.10 | The Cancer Genome Atlas (TCGA) public dataset analysis

Pearson correlation analysis was conducted using the powerful online tool GEPIA [20] (http://gepia.cancer-pku.cn/) to investigate the association between the infiltration abundance of DC_LAMP3 cells and that of CD4_Tregs/CD8_T ex cells in the cervical and endocervical cancer (CESC) dataset from the TCGA database downloaded from Xena (https://xena.ucsc.edu/). A non-log scale was used for the calculations, and a log-scale axis was used for visualization.

2.11 | TCR-seq clonotype expansion analysis

scTCR-seq data were processed using Cell Ranger (version 5.0.1, 10x Genomics) against mouse V(D)J as a reference provided by 10x Genomics. We maintained cells with at least one productive TCR a or TCR b chain for subsequent analyses, such as analyses of the distribution of complementary determining region 3 (CDR3) length, usage patterns of VDJ gene segments and combinations, and diversity of the TCR repertoire. In each sample, if two or more cells had identical α-β pairs, these T cells were identified as clonal T cells, and they shared a unique clonotype ID. To integrate the TCR results with gene expression data, a TCR-based analysis was performed only for cells identified as T cells. We identified the T-cell clonotypes that were shared among the clusters or samples.

2.12 | Multicolor IHC staining

To elucidate the spatial localization of DC_LAMP3, CD4_Treg, and CD8_T ex cells, we conducted multicolor IHC staining assays using the Multiplex IHC kit (mIHC-3271-6, Absin, Shanghai, China) according to the manufacturer's instructions. The slides were incubated with a blocking antibody diluent at room temperature (25°C) for 10 min and subsequently incubated overnight at 4°C with primary antibodies applied sequentially. The slides were subsequently incubated with a secondary antibody (HRP polymer, anti-mouse/rabbit IgG; Abcam, Cambridge, UK) at room temperature for 10 min. Next, a fluorophore (tyramide signal amplification plus working solution) was

applied to the sections, followed by microwave heat treatment. The nuclei were stained with DAPI (Beyotime, Shanghai, China) after all antigens were labeled. Multispectral images of each stained slide were captured using the Mantra system (PerkinElmer, Waltham, MA, USA). The primary antibodies used were anti-CD3 (Dilution at 1:200; 85061, CST, Danvers, MA, USA), anti-CD4 (1:200; 48274, CST, Danvers, MA, USA), anti-CD8A (1:200; 85336, CST, Danvers, MA, USA), anti-CD80 (1:1000; ab134120, Abcam, Cambridge, UK), anti-PD1 (1:200; 86163, CST, Danvers, MA, USA), anti-PD-L1 (1:100; 13684, CST, Danvers, MA, USA), and anti-IDO1 (1:100; ab211017, Abcam, Cambridge, UK).

2.13 | Animal experiments

All animal experiments were approved by the Fudan University Animal Care and Use Committee. Female C57BL/6 mice (5-6 weeks old) were purchased from the Laboratory Animal Center of the Shanghai Institutes for Biological Sciences (Shanghai, China) and housed in a pathogen-free environment. To establish ectopic tumors, 1×10^6 TC-1 cells (in 200 μL of PBS) were subcutaneously injected into the right shoulders of the C57BL/6 mice. When the tumor volume reached approximately 50 mm^3 (denoted as day 0), the tumor-bearing mice were randomly divided into 10 groups ($n = 6$ in each group): control, anti-PD-1, anti-CTLA4, anti-TIGIT, anti-TIM3, epacadostat (E), anti-PD-1 + E, anti-CTLA4 + E, anti-TIGIT + E, and anti-TIM3 + E groups. The transplant recipients received 200 μg of anti-PD-1 (Cat.No.BE0146, Bioxcell, West Lebanon, N.H, USA), anti-CTLA4 (BE0032, Bioxcell), anti-TIGIT (BE0274, Bioxcell), or anti-TIM3 agents (BE0115, Bioxcell) twice a week × 4 doses (Day 3, Day 6, Day 9, and Day 12) through intraperitoneal injection. The IDO1 inhibitor epacadostat (200 mg/kg; MedChemExpress, NJ, USA) was administered daily by gavage from day 0 to 12. Tumor size was monitored every 3 days and measured at the time of sacrifice, and the volume was calculated as ($1/2 \times$ length $\times$ width^2). Peripheral blood was collected from each mouse and leukocytes were isolated using a red blood cell lysis solution (Beyotime Biotechnology, Shanghai, China) for flow cytometry analysis.

2.14 | Flow cytometry

Single-cell blood suspensions were washed twice with PBS and incubated for 30 min in the dark with antibodies against specific surface proteins. To detect intracellular proteins, cells were stimulated for 6 h with 10 μg/mL brefeldin A and 2 μmol/L ionomycin (Absin, Shanghai, China) before staining. The cells were then fixed and permeabilized using a fixation/permeabilization wash buffer (BioLegend, San Diego, CA, USA) and stained with antibodies for 30 min in the dark. For Ki67 staining, cells were incubated in 70% ethanol for 1 h at -20°C and subsequently stained with an anti-Ki67 antibody (1:1000; 563757, BD Biosciences, San Jose, CA, USA). All antibodies used for flow cytometry are listed in Supplementary Table S2. All samples were run on a CytoFLEX platform (Beckman Coulter, Bria, CA, USA) and analyzed using the FlowJo version 10.8 software (BD Biosciences).

2.15 | Quantification and statistical analysis

Specific statistical tests and metrics (mean value ± standard deviation [SD] or median value with 95% confidence interval [CI]) used for comparisons, along with sample sizes, are described in the Results section and the figure legends. Comparisons of continuous data of different data types between the two groups were performed using the unpaired two-tailed Student's t-test, Mann-Whitney test, or Kruskal-Wallis test, while one-way ANOVA with Tukey's post hoc test was used to compare data between multiple groups. All statistical analyses were performed using GraphPad Prism, version 8 (GraphPad Software, La Jolla, CA, USA). Statistical significance was set at $P < 0.05$.

3 | RESULTS

3.1 | Malignant cervical epithelial cells exhibited no remarkable signs of tumor escape

To investigate the molecular mechanisms underlying tumor immune escape during CC development, we performed scRNA-seq using 17 clinical samples, including normal cervical tissues, HSIL foci, and CC tissues (Supplementary Table S1). Having captured 119,351 cells and performed routine data processing, we obtained 32 cell subpopulations by unsupervised clustering and further categorized them into the following 11 cell types according to well-known marker genes [21]: epithelial cells (*EPCAM* and *KRT18*), endothelial cells (*VWF* and *PLVAP*), fibroblasts (*COL1A1* and *LUM*), smooth muscle cells (*ACTA2* and *TAGLN*), neutrophils (*CSF3R*), mast cells (*CPA3*), monocytes (*FCN1*), macrophages (*C1QB* and *LYZ*), dendritic cells (DCs) (*IRF8*), B/plasma cells (*JCHAIN* and *MZB1*), and T cells (*CD2* and *CD3D*) (Figure 1A-B, Supplementary Figure S1A).

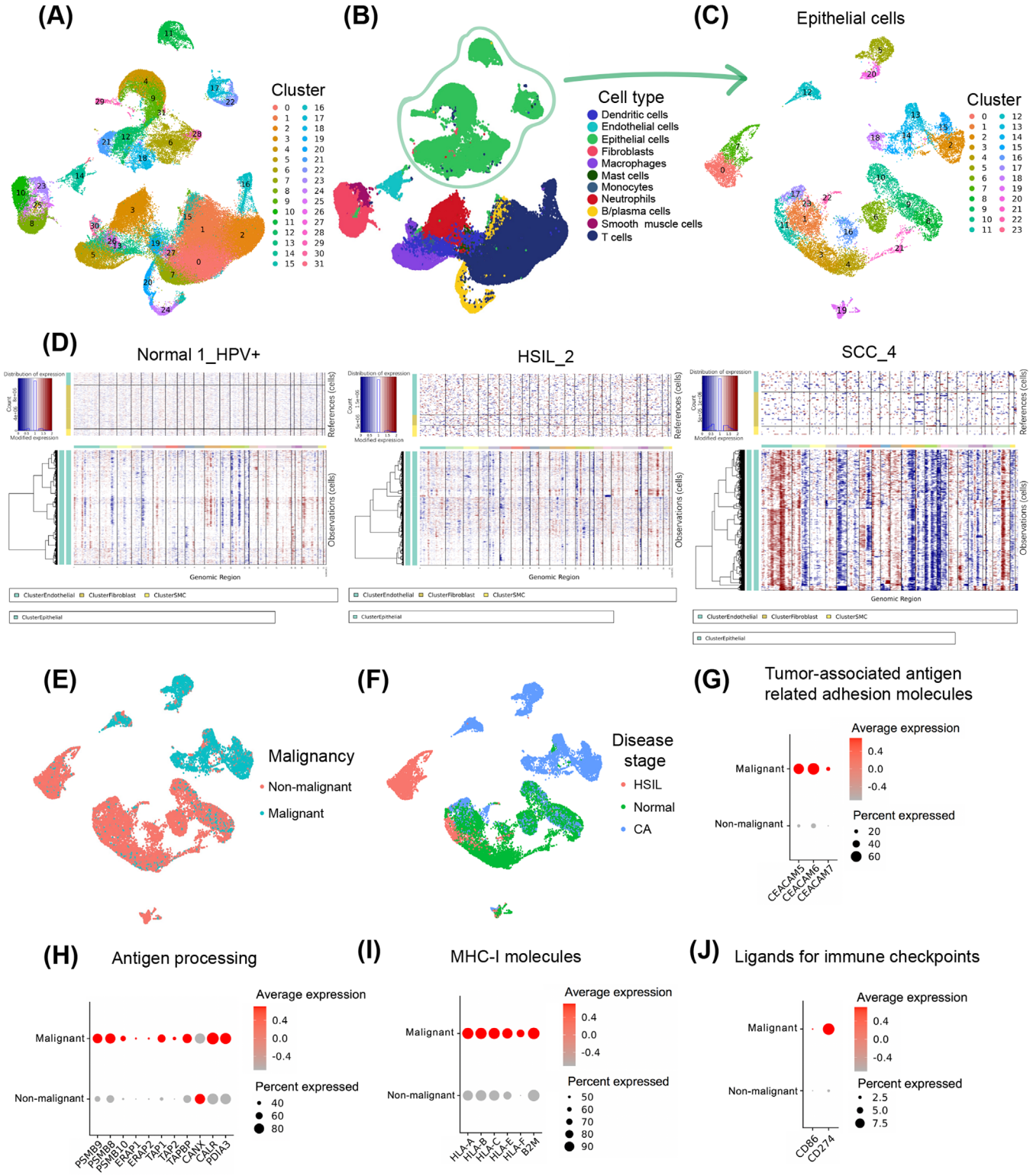

FIGURE 1 Malignant cervical epithelial cells exhibit no remarkable signs of tumor escape. (A) UMAP projection of 119,351 cells from 17 clinical samples consisting of normal cervical tissues, HSIL foci, and CC tissues that were clustered into 32 clusters. Each dot corresponds to a single cell and is colored according to the cell cluster. (B) UMAP projection of 119,351 cells, which were further categorized into 11 major cell types. Each dot, which corresponds to a single cell, is colored according to cell type. See also Supplementary Figure S1A. (C) UMAP projection of the 24 epithelial subclusters generated from unsupervised reclustering. Each dot, which corresponds to a single epithelial cell, is colored according to subcluster. See also Supplementary Figure S1B. (D) CNV profiles of epithelial cells inferred from scRNA-seq of normal cervical tissues (N1 with HPV infection [Normal 1_HPV+]), HSIL_2, and SCC_4 data. Red and blue indicate chromosomal amplifications and deletions, respectively. (E) UMAP projection of all epithelial cells presenting as malignant (light blue) and non-malignant (red). (F) UMAP

First, we focused on epithelial cells, which are the major components of the CC. Based on unsupervised clustering, we identified 24 epithelial cell clusters (Figure 1C, Supplementary Figure S1B). To further understand the malignant transition of epithelial cells during cervical carcinogenesis, we evaluated CNV in epithelial cells from each clinical sample using inferCNV analysis. We discovered considerably greater substantial DNA fragment amplification and deletion in CC-derived epithelial cells, representing a higher neoantigen burden and greater malignancy, compared with that in epithelial cells originating from the normal cervical tissues or HSIL foci (Figure 1D-F).

We compared malignant and non-malignant cervical epithelial cells to determine whether malignant cervical epithelial cells evade recognition and eradication of the immune system by mechanisms such as antigen modulation, defects in the antigen-processing machinery, downregulation of major histocompatibility complex (MHC)-I molecules, or upregulation of ligands for well-known immune checkpoints [22]. Regarding antigen modulation, the expression of tumor-associated antigen-related adhesion molecules (Carcinoembryonic Antigen Related Cell Adhesion Molecules: *CEACAM5*, *CEACAM6*, and *CEACAM7*) was higher in malignant cervical cells, demonstrating no specific signs of antigen depletion at the mRNA level (Figure 1G); however, determining whether antigen modulation occurs at the genomic or posttranslational level requires further investigation. Regarding antigen-processing machinery, critical genes involved in antigen processing (including Proteasome Subunit Beta: *PSMB 8/9/10*, Endoplasmic Reticulum Aminopeptidase: *ERAP1/2*, The Antigen Processing genes: *TAP1/2*, and Tapasin Binding Protein: *TAPBP*) were more highly expressed in malignant epithelial cells (Figure 1H), potentially indicating a strengthened antigen-processing effect as feedback for CC oncogenesis, instead of functional depletion. *MHC-I* (*HLA-A/B/C/E/F*) and the related component *B2M* were upregulated in malignant epithelial cells rather than being unexpressed (Figure 1I). Regarding the ligands (*CD86* and *CD274*) for well-known immune checkpoints (CTLA4 and PD-1), a higher expression was observed in malignant epithelial cells than in non-malignant cells; however, no more than 10% of malignant epithelial cells expressed *CD274* or *CD86* (Figure 1J). The above findings showed that malignant cervical epithelial cells retained their immunogenicity and revealed few defects in antigen processing and that they did not show downregulation of MHC-I or extensive upregulation of ligands for known immune checkpoints. In summary, signs of immune escape were not apparent in malignant cervical epithelial cells.

Tumor immune suppression is generally associated with not only tumor escape but also dysfunctional antigen-presenting cells (APCs) and immune effector cells [23]. Therefore, we subsequently focused on DCs, which are professional APCs, to further explore the significant events that DCs experience during CC development and determine whether DCs regulate CC immune evasion.

3.2 | LAMP3$^+$ DCs: mature DCs with immunoregulatory effects that participate in tryptophan metabolism

We acquired 9 DC clusters by re-clustering and categorized them into the following 6 subsets according to marker gene expression [24] (Figure 2A-B, Supplementary Figure S2A): DC_CD207_CD1C (*CD207* and *CD1C*), DC_CD1C (*CD1C, FCER1A, CLEC10A*), DC_CLEC9A (*CLEC9A, XCR1, CADM1*), pDC (*LILRA4*), DC_cycling (*MKI67*), and DC_LAMP3 (*LAMP3*). According to the classic DC markers, DC_CD207_CD1C and DC_CD1C cells, which express high levels of *CD1C*, *FCER1A*, and *CLEC10A*, corresponded to cDC2s, which is responsible for antigen presentation on MHC-II molecules for CD4$^+$ T-cell priming. DC_CLEC9A cells, which specifically expressed *CLEC9A*, *XCR1*, and *CADM1*, corresponded to cDC1s, which specialize in the cross-presentation of antigens onto MHC-I molecules for CD8$^+$ T-cell priming. In addition, DC_cycling cells, which highly expressed genes closely related to the cell cycle, such as TOP2A and MKI67, demonstrated extensive proliferation and expansion. Notably, DC_LAMP3 cells did not correspond to any classic DC subpopulation based on well-recognized markers. To further identify the differences and relationships between DC_LAMP3 cells and other DC subpopulations, we conducted pseudotime and CytoTrace analyses (Figures 2C, Supplementary Figure S2B) and discovered that DC_LAMP3 cells were terminally

projection of all epithelial cells presenting at different disease stages, including those in the normal cervix (N), HSIL, and CA (cancer). Each dot, which corresponds to a single cell, is colored according to disease stage. (G-J) Dot plot indicating the average expression levels and proportions of cells expressing tumor-associated antigen-related adhesion molecules (G), antigen processing-related genes (H), MHC-I molecules (I), and ligands for immune checkpoints (J) in malignant and non-malignant epithelial cells. The colors represent the average expression levels, and dot sizes represent the percent expression of selected genes. Abbreviations: UMAP, Uniform Manifold Approximation and Projection; HSIL, high-grade squamous intraepithelial lesion; CNV, copy number variation; scRNA-seq, single-cell RNA sequencing; HPV, human papillomavirus; SCC, squamous cell carcinoma; MHC, major histocompatibility complex.

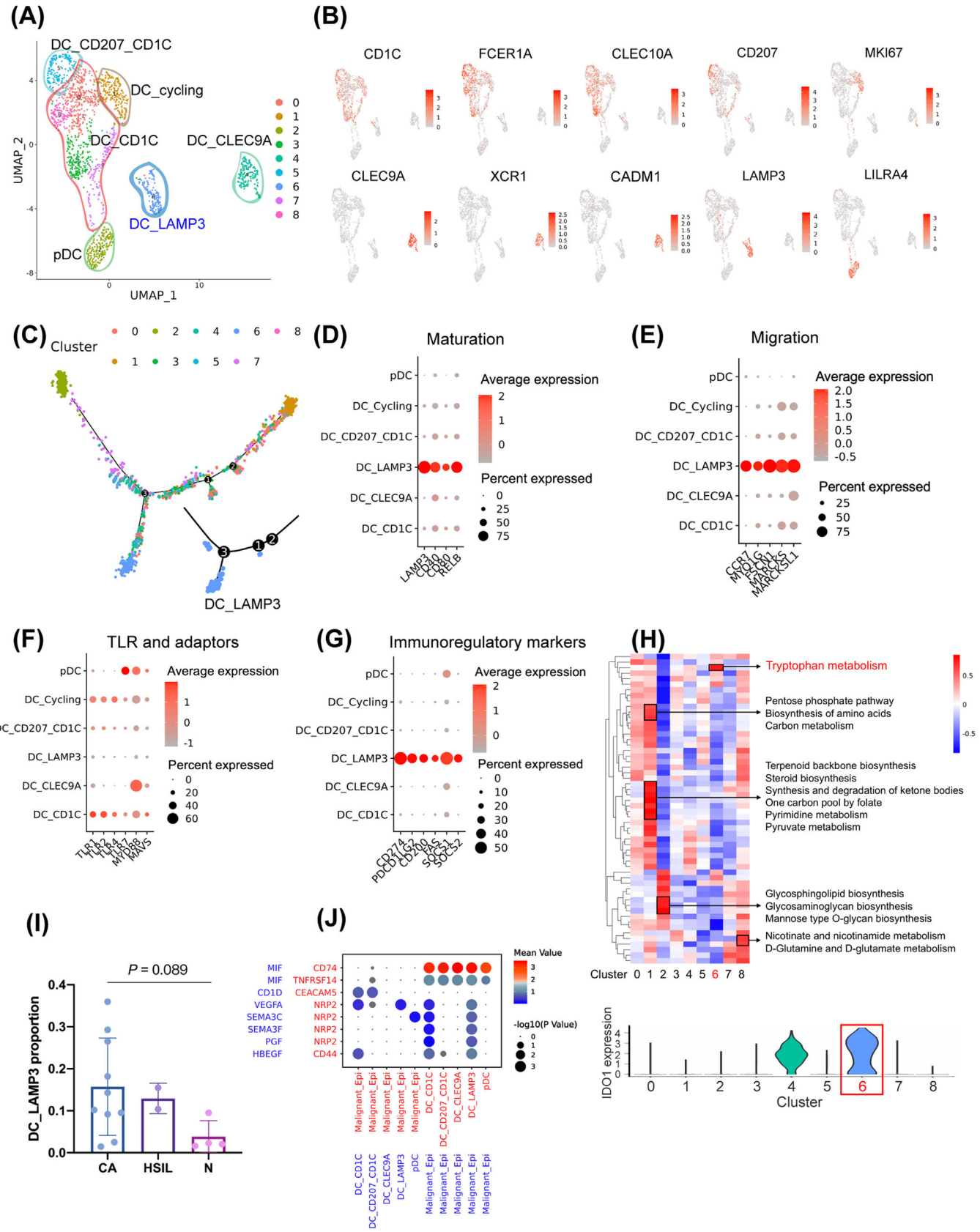

FIGURE 2 Mature LAMP3$^+$ DCs exert immunoregulatory effects and participate in tryptophan metabolism in the CC TME. (A) UMAP projection of the 9 subclusters of DCs generated from unsupervised clustering, which were categorized into 6 main groups according to marker gene expression. (B) Marker gene expression plotted onto the UMAP projection: *CD1C*, *FCER1A*, and *CLEC10A* for DC_CD1C (subcluster 0, 3, 7, 8) and *CD207* for DC_CD207_CD1C (subcluster 5); *MKI67* for DC_cycling (subcluster 1); *CLEC9A*, *XCR1*, and *CADM1* for

differentiated DCs derived from both cDC1s (DC_CLEC9A) and cDC2s (DC_CD207_CD1C and DC_CD1C). Accordingly, DC_LAMP3 cells were characterized by the specific expression of maturation markers, such as *LAMP3*, *CD40*, *CD80*, and *RELB* (Figure 2D).

Next, we explored the molecular functions of DC_LAMP3 cells. Notably, DC_LAMP3 cells demonstrated migrative ability with a high expression of *CCR7*, *MYO1G*, *FSCN1*, *MARCKS*, and *MARCKSL1* (Figure 2E). In addition, compared with other cDCs, DC_LAMP3 cells exhibited a significantly lower expression of Toll-like receptors (TLRs) and their adaptors (*TLR1*, *TLR2*, *TLR4*, *TLR7*, *MYD88*, and *MAVS*) (Figure 2F) and higher expression of immunoregulatory markers (*CD274*, *PDCD1LG2*, *CD200*, *FAS*, *SOCS1*, and *SOCS2*) (Figure 2G), indicating inhibitory immune regulation by DC_LAMP3 cells. Furthermore, DC_LAMP3 cells expressing high levels of IDO1 actively participated in tryptophan metabolism (Figure 2H), which was reported to be associated with immune suppression [25, 26].

Considering that DC_LAMP3 cells tended to be more abundant in tissues from the CC group than in precancerous lesions and normal cervical tissues (Figure 2I), we inferred that DC_LAMP3 cells might be closely associated with cervical malignant transition. Subsequently, we further investigated the cellular interactions between malignant epithelial cells and DCs, especially DC_LAMP3 cells (Figure 2J). Notably, we found no CEACAM5-CD1D interaction mediating the recognition and presentation of self-antigens between malignant cervical epithelial cells and DC_LAMP3 cells; however, we observed a remarkable interaction between malignant cervical epithelial cells and cDC1 cells. This finding implied an impaired antigen presentation in mature DC_LAMP3 cells, which potentially facilitates CC immune escape. Furthermore, we identified a VEGFA/SEMA3F/SEMA3C/PGF-NRP2 interaction between malignant cervical epithelial cells and DC_LAMP3 cells, which synergistically stimulated angiogenesis and tumorigenesis [27–29].

These findings revealed the mature state, immunoregulatory effect, and role of DC_LAMP3 cells in tryptophan metabolism, indicating impaired antigen processing and presentation. However, further exploration is required to determine how DC_LAMP3 cells communicate with other immune cells, especially T cells, thus modulating CC immune escape.

3.3 | CD8$^+$ reactive T cells in CC microenvironment mainly exhibited dysfunction and exhaustion

Before investigating the cellular crosstalk between DC_LAMP3 and T cells, we investigated the molecular features and biological functions of T cells within the cervical immune microenvironment. After unsupervised re-clustering, 11 CD8$^+$ T-cell clusters were further grouped into 7 types as follows [30] (Figure 3A-B, Supplementary Figure S3A): CD8_Naive (*CCR7* and *LEF1*), CD8_recently activated effector memory or effector T cells(CD8_Temra/eff) (*CX3CR1* and *FGFBP2*), CD8_mucosa-associated invariant T cells (CD8_MAIT) (*IL7R* and *KLRB1*), CD8_resident memory T cells (CD8_Trm) (*CAPG* and *XCL1*), CD8_effector memory T cells (CD8_Tem) (*GZMK* and *CXCR4*), CD8_exhausted T cells (CD8_Tex) (*CXCL13* and *HAVCR2*), and CD8_Cycling (*MKI67* and *TOP2A*). Regarding the proportion of different CD8$^+$ T cell types in the normal cervical tissues, HSILs, and CC tissues, we observed that CD8_Trm cells extensively infiltrated into the normal cervical and HSIL tissues, whereas CD8_Tex cells were abundant in the CC group (Supplementary Figure S3B).

DC_CLEC9A (subcluster 4); *LILRA4* for pDC (subcluster 2); *LAMP3* for DC_LAMP3 (subclusters 6). The color gradation from grey to red indicates relative expression levels from low to high, respectively. (C) Differentiation trajectory of DC subclusters predicted by Monocle indicating the terminal location of DC_LAMP3 cells. (D-G) Dot plot indicating the average expression levels and proportion of cells expressing maturation markers (D), migration markers (E), TLRs and adaptors (F), and immunoregulatory markers (G) in the 6 main DC groups. The colors represent the average expression levels, and dot sizes represent the percent expression of selected genes. (H) Heatmap demonstrating the QuSAGE enrichment scores for the metabolic pathways for each DC subcluster (upper) and a violin plot showing expression of the IDO1 gene in each DC subcluster (lower). In the heatmap, a score of 0 (white) indicates nonsignificant enrichment after FDR correction, whereas red and blue indicate positive and negative associations, respectively. (I) Scatter plots indicating the proportions of DC_LAMP3 cells among all DCs in 3 disease stages, including cervical CA (cancer), HSIL, and N (normal cervix). Error bar: median value with 95%CI ($n = 17$ standing for 17 CC samples). *P* values were obtained by the Kruskal-Wallis test ($P = 0.089$). (J) Dot plots demonstrate selected ligand-receptor interactions between different DC groups and malignant cervical epithelial cells. The involved cell types and ligand-receptor interactions are indicated by columns and rows, respectively. The means of the average expression levels of two interacting molecules are indicated by the color key, with blue to red representing low to high expression, respectively. The [-Log10(*P* values)] are indicated by dot size. Abbreviations: DCs, dendritic cells; CC, cervical cancer; TME, tumor microenvironment; TLR, toll-like receptor; CI, confidence interval.

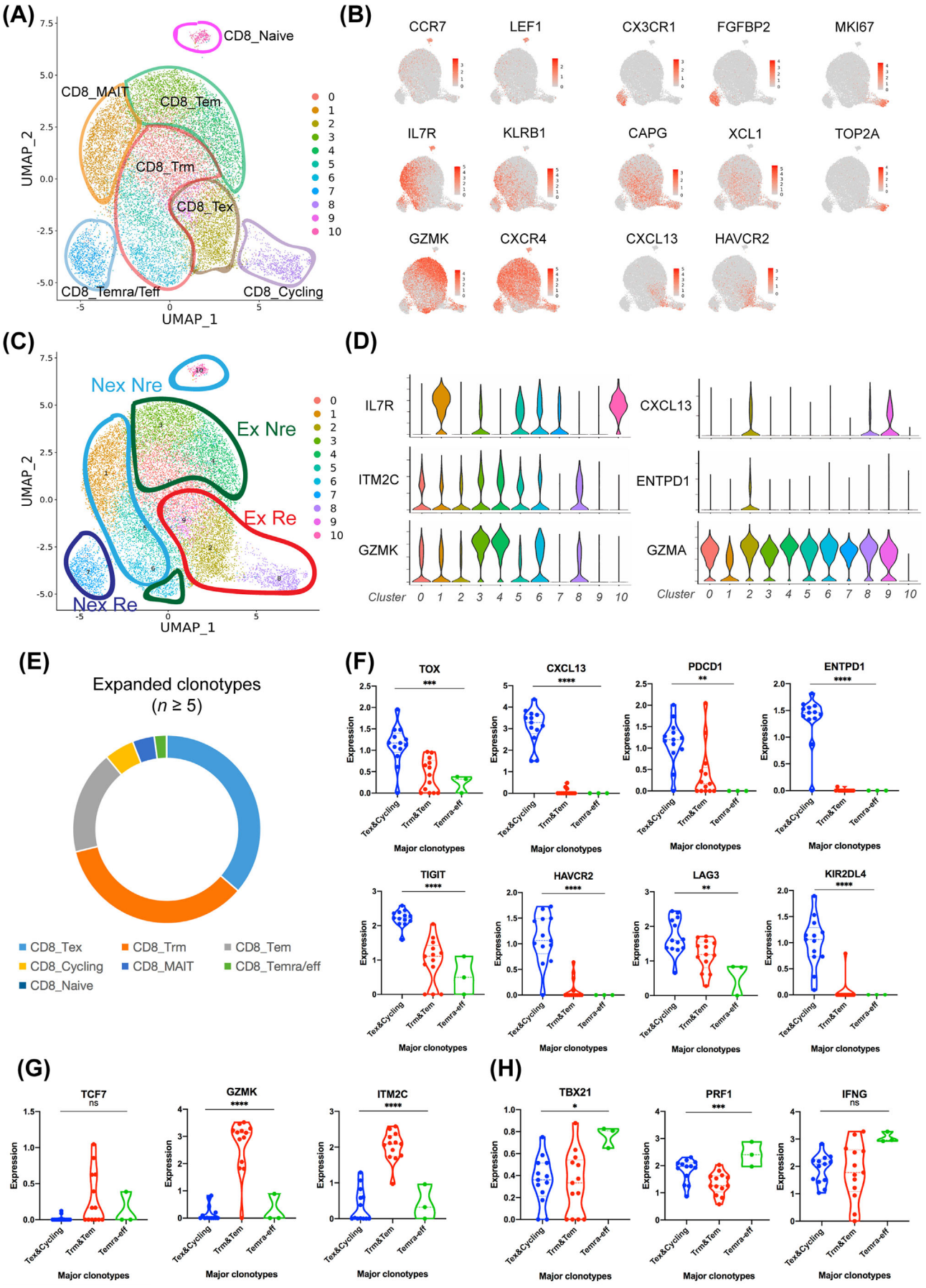
(A)
CD8_Naive
CD8_MAIT
CD8_Tem
CD8_Trm
CD8_Tex
CD8_Temra/Teff
CD8_Cycling
UMAP_1
UMAP_2
(B)
CCR7
LEF1
CX3CR1
FGFBP2
MKI67
IL7R
KLRB1
CAPG
XCL1
TOP2A
GZMK
CXCR4
CXCL13
HAVCR2
(C)
Nex Nre
Ex Nre
Ex Re
Nex Re
(D)
IL7R
ITM2C
GZMK
CXCL13
ENTPD1
GZMA
Cluster 0 1 2 3 4 5 6 7 8 9 10
(E)
Expanded clonotypes
(n ≥ 5)
CD8_Tex
CD8_Trm
CD8_Tem
CD8_Cycling
CD8_MAIT
CD8_Temra/eff
CD8_Naive
(F)
TOX
CXCL13
PDCD1
ENTPD1
TIGIT
HAVCR2
LAG3
KIR2DL4
Expression
Major clonotypes
Tex&Cycling
Trm&Tem
Temra-eff
(G)
TCF7
GZMK
ITM2C
(H)
TBX21
PRF1
IFNG

According to Zheng *et al.* [13], which integrated in vitro immunological screening and scRNA sequencing, CD8$^+$ T cells can be categorized into 3 subtypes according to immune exhaustion and neoantigen reactivity: (1) immune non-exhausted and neoantigen non-reactive CD8$^+$ T cells (Nex Nre; *IL7R*), (2) immune exhausted and neoantigen non-reactive CD8$^+$ T cells (Ex Nre; *GZMK* and *ITM2C*), and (3) immune exhausted and neoantigen reactive CD8$^+$ T cells (Ex Re; *CXCL13*, *ENTPD1* and *GZMA*). Intriguingly, we found that in the present study (Figure 3C-D), CD8_Naive cells (cluster 10), CD8_MAIT cells (cluster 1), and some CD8_Trm cells (cluster 5) may have corresponded to immune non-exhausted and neoantigen non-reactive CD8$^+$ T cells, and CD8_Tem cells (clusters 3 and 4) and some CD8_Trm cells (cluster 6) may have corresponded to immune exhausted and neoantigen non-reactive CD8$^+$ T cells, while most CD8_Tex cells and CD8_cycling cells, particularly abundant in CC, probably corresponded to immune exhausted and neoantigen reactive CD8$^+$ T cells. Furthermore, TCR analysis (Figure 3E-G) indicated that CD8_Tex cells with high expression of *TOX*, *CXCL13*, *PDCD1*, *ENTPD1*, *TIGIT*, *HAVCR2*, *LAG3*, and *KIR2DL4* exhibited the greatest clonal expansion, highlighting both tumor antigen reactivity and attenuation of anti-tumor immunity. Additionally, CD8_Trm and CD8_Tem cells showed relatively abundant TCR clonotypes but probably no tumor neoantigen-associated clonotypes, which are characterized by low expression of *CXCL13* and high expression of *GZMK*.

However, CD8_Temra/eff cells (cluster 7), which were characterized by a high expression of *GZMA* but no expression of *CXCL13* (Figure 3D), did not belong to the above 3 subtypes. Therefore, we hypothesized that CD8_Temra/eff cells are immune non-exhausted and neoantigen reactive (Nex Re; Figure 3C) CD8$^+$ T cells that function as effector T cells. TCR analysis indicated that the CD8$^+$ Temra/eff cells did not have extensively expanded TCR clonotypes. However, clonally expanded CD8_Temra/eff cells expressed high levels of *TBX21* (a transcription factor closely related to immune reaction-activating Th1 genetic programs), *PRF1* (perforin 1, involved in defense against neoplastic cells), and *IFNG* (type II interferon, involved in antimicrobial, antiviral, and antitumor responses by activating effector immune cells and enhancing antigen presentation) but hardly expressed immune checkpoints representing immune exhaustion (Figure 3F and H), which supported our hypothesis that CD8_Temra/eff cells in our study might be immune non-exhausted and neoantigen reactive CD8$^+$ T cells.

We identified 4 types of CD8$^+$ T cells in the CC microenvironment: immune non-exhausted and neoantigen non-reactive, immune exhausted and neoantigen non-reactive, immune non-exhausted and neoantigen reactive, and immune exhausted and reactive cells. Strikingly, most neoantigen-reactive CD8$^+$ T cells in the CC TIME had already become dysfunctional and exhausted, whereas only a minority exhibited effective immune function. Therefore, stimulating neoantigen reactivity and restoring the anti-tumor cytotoxicity of CD8$^+$ T cells are major strategies in the development of novel cancer immunotherapies.

3.4 | CD4$^+$ reactive T cells in CC microenvironment: helpers and regulators

We further characterized CD4$^+$ T cells based on unsupervised clustering and marker gene expression [30] (Figure 4A, Supplementary Figure S3C).Among them are the well-known CD4_regulatory T cells (CD4_Tregs) (*FOXP3*, *IL2RA*, and *CTLA4*), which exert immunoregulatory effects, and helper CD4_T cells (CD4_Th cells), including both CD4_effector memory/type 1-like helper CD4_T cells (CD4_Tem/Th1-like cells) (CXCL13 and IFNG) and Th1-like cells (*CXCL13* and *CD200*), which assist cytotoxic CD8$^+$ T lymphocytes in antitumor

FIGURE 3 CD8$^+$ reactive T cells in the CC microenvironment mainly exhibit dysfunction and exhaustion. (A-B) UMAP projection of the 11 subclusters of CD8$^+$ T cells generated from unsupervised reclustering, which could be categorized into 7 main groups (A) according to marker gene expression (B): *CCR7* and *LEF1* for CD8_naive (subcluster 10); *CX3CR1* and *FGFBP2* for CD8_Temra/eff (subcluster 7); *IL7R* and *KLRB1* for CD8_MAIT (subcluster 1); *CAPG* and *XCL1* for CD8_Trm (subcluster 0, 5, and 6); *GZMK* and *CXCR4* for CD8_Tem (subcluster 3 and 4); *CXCL13* and *HAVCR2* for CD8_ Tex (subcluster 2 and 9); and *MKI67* and *TOP2A* for CD8_Cycling (subcluster 8). The color key from grey to red indicates relative expression levels from low to high, respectively. (C) UMAP projection of the 11 subclusters of CD8$^+$ T cells presenting as Nex Nre cells (light blue), Nex Re cells (purple), Ex Nre cells (green), and Ex Re cells (red). (D) Violin plot showing the gene expression of *IL7R*, *ITM2C*, *GZMK*, *CXCL13*, *ENTPD1*, and *GZMA* in each CD8$^+$ T subcluster. (E) Pie graph illustrating the proportions of different subgroups among the CD8$^+$ T cells that had more than 5 expanded clonotypes ($n \geq 5$). Each color corresponds to one CD8$^+$ T subgroup. (F-H) Violin plots indicating the expression levels of genes associated with immune exhaustion and tumor reactivity (F), exhaustion but nonreactivity (G), and a positive immune reaction (H) in different groups of CD8$^+$ T cells with major expanded clonotypes. *P* values were obtained by one-way ANOVA or Kruskal-Wallis test. *, $P < 0.05$; **, $P < 0.01$; ***, $P < 0.001$; ****, $P < 0.0001$. Abbreviations: Nex, non-exhausted; Nre, non-reactive to tumor antigen; Re, reactive to tumor antigen; Ex, exhausted; ns, not significant.

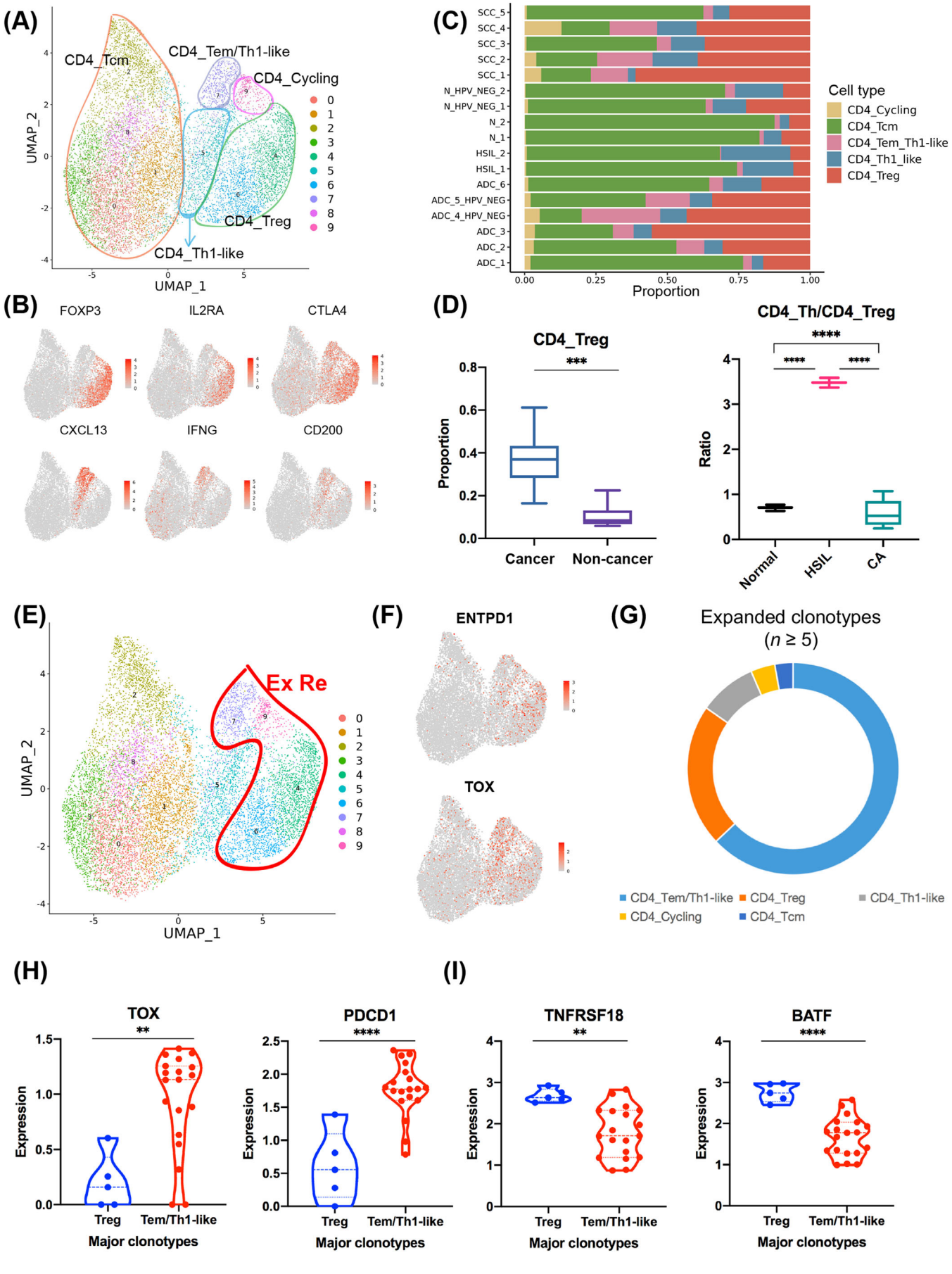
(A)
CD4_Tcm
CD4_Tem/Th1-like
CD4_Cycling
CD4_Treg
CD4_Th1-like
UMAP_1
UMAP_2
(B)
FOXP3
IL2RA
CTLA4
CXCL13
IFNG
CD200
(C)
SCC_5
SCC_4
SCC_3
SCC_2
SCC_1
N_HPV_NEG_2
N_HPV_NEG_1
N_2
N_1
HSIL_2
HSIL_1
ADC_6
ADC_5_HPV_NEG
ADC_4_HPV_NEG
ADC_3
ADC_2
ADC_1
Proportion
Cell type
CD4_Cycling
CD4_Tcm
CD4_Tem_Th1-like
CD4_Th1_like
CD4_Treg
(D)
CD4_Treg
Proportion
Cancer
Non-cancer
CD4_Th/CD4_Treg
Ratio
Normal
HSIL
CA
(E)
Ex Re
UMAP_1
UMAP_2
(F)
ENTPD1
TOX
(G)
Expanded clonotypes
(n ≥ 5)
CD4_Tem/Th1-like
CD4_Treg
CD4_Th1-like
CD4_Cycling
CD4_Tcm
(H)
TOX
PDCD1
Expression
Treg
Tem/Th1-like
Major clonotypes
(I)
TNFRSF18
BATF

immunity (Figure 4B). By comparing the proportions of different CD4$^+$ T-cell subsets in normal cervical tissues, HSIL foci, and CC tissues (Figure 4C), we found that CD4_Tregs remained in balance with CD4_Th cells in terms of infiltration in the normal cervical tissues; however, they were less abundant than CD4_Th cells in HSIL foci (Treg/Th <1), and they outnumbered CD4_Th cells in CC tissues (Treg/Th >1) (Figure 4D). Hence, we hypothesized that once the balance between CD4$^+$ Th cells and Tregs is disrupted, cervical lesions are likely to progress to malignancy.

Interestingly, we observed that most CD4_Tem/Th1-like cells and CD4_Tregs (clusters 7, 9, 4, and 6) in our study tended to be immune exhausted and neoantigen-reactive CD4$^+$ T cells, as defined in Zheng *et al.* [13], which characterized marker genes, such as *ENTPD1* and *TOX* (Figure 4E-F). TCR analysis confirmed that CD4_Tem/Th1-like cells and CD4_Tregs exhibited the greatest TCR clonotype expansion (Figure 4G). This result indicated that although they demonstrated functional heterogeneity, CD4_Tem/Th1-like cells, which assist in anti-tumor immunity, and CD4_Tregs, which negatively modulate the immune response, were probably neoantigen-reactive with clonotype expansion. Intriguingly, clonally expanded CD4_Tem/Th1-like cells (helper immune exhausted and neoantigen reactive CD4$^+$ T cells) exhibited greater immune exhaustion, considering the expression levels of *TOX* and *PDCD1* (Figure 4H), while clonally expanded CD4_Tregs (regulatory immune exhausted and neoantigen reactive CD4$^+$ T cells) played a crucial role in T cell differentiation and activation, with upregulation of *TNFRSF18* and *BATF* expression (Figure 4I).

These findings indicated that a sophisticated balance between helper and regulatory reactive CD4$^+$ T cells was valuable for CC therapy. In particular, relieving the exhaustion of CD4$^+$ T helper cells and inhibiting the effects of CD4$^+$ T regulators should be considered.

3.5 | DC_LAMP3 cells communicated synergistically with both reactive CD8_Tex cells and CD4_Tregs to mediate CC immune escape

Having described the features and functions of reactive T cells in the CC microenvironment, we focused on the association and interactions between DCs and neoantigen-reactive T cells. Notably, we found a positive association in terms of cell abundance between DC_LAMP3 cells, CD8_Tex cells, and CD4_Tregs; these correlations also existed in the TCGA CESC dataset, indicating a potential close interaction (Figure 5A-B).

Regarding the cellular crosstalk between DCs and CD8_Tex cells, the mean expression of ligand-receptor pairs related to immune checkpoints (CD274/PDCD1LG2-PDCD1, CD80/CD86-CTLA4, LGALS9-HAVCR2, PVR-CD96, and PVR/NECTIN2-TIGIT) was basically higher in LAMP3$^+$ DCs and CD8_Tex cells than in other DC subpopulations and CD8_Tex cells, highlighting the immunoregulatory effects of DC_LAMP3 cells (Figure 5C). In addition, by comparing ligand-receptor interactions in tissues representing different disease stages, including normal cervical tissues, HSIL, and CC tissues (Figure 5D), we hypothesized that immune surveillance and tolerance occur in the normal cervical tissues, a positive immune reaction occurs in HSILs, and immune suppression occurs in CC tissues. In particular, the cellular interactions between immune inhibitory checkpoints, such as CD80/CD86-CTLA4, LGALS9-HAVCR2, PVR/NECTIN2-TIGIT, and CD274/PDCD1LG2-PDCD1, remained at a low level in the normal cervical tissues, indicating immune tolerance and surveillance, probably because of initial microbial infection such as human papillomavirus (HPV) infection. These interactions were even less detectable in HSIL, revealing a positive immune reaction, but considerably more pronounced in CC tissues, indicating immune

FIGURE 4 CD4$^+$ reactive T cells in the CC microenvironment could be divided into helpers and regulators. (A-B) UMAP projection of the 10 subclusters of CD4$^+$ T cells generated from unsupervised reclustering, which could be categorized into 5 main groups: (A) with marker gene expression; (B) *FOXP3*, *IL2RA*, and *CTLA4* for CD4_Tregs (subclusters 4 and 6); *CXCL13*, *IFNG*, and *CD200* for Tem/Th1-like cells (subcluster 7) and Th1-like cells (subcluster 5). The color gradation from grey to red indicates relative expression levels from low to high, respectively. (C) Histogram indicating the ratios of each CD4$^+$ T-cell type in the 17 samples, including normal cervical tissues, HSIL, and CC tissues, including both SCC and ADC. (D) Box plots indicating the proportion of CD4_Tregs among all CD4$^+$ T cells in the cancer group compared to the noncancer group (left panel) and the ratio between CD4_Th cell and Treg abundance in the normal cervix, HSIL, and cancer (CA) groups (right panel). Error bar: median value with 95%CI ($n = 17$ representing 17 clinical samples altogether). *P* values were obtained by Student's t test and one-way ANOVA with Tukey's multiple comparison test, respectively. ***, $P < 0.001$; ****, $P < 0.0001$. (E) UMAP projection of potential Ex Re CD4$^+$ T cells (red). (F) Gene expression of *ENTPD*1 and *TOX* plotted onto the UMAP projection. (G) Pie graph illustrating the proportions of different subgroups among the CD4$^+$ T cells that had more than 5 expanded clonotypes ($n \geq 5$). Each color corresponds to one CD4$^+$ T cell subgroup. (H-I) Violin plots indicating the expression levels of genes associated with immune exhaustion (H) and differentiation and activation (I) in CD4_Tregs compared with that in CD4_Tem/Th1-like cells with major expanded clonotypes. *P* values were obtained by Student's t test. **, $P < 0.01$; ****, $P < 0.0001$. Abbreviations: HSIL, high-grade squamous intraepithelial lesion; CC, cervical cancer; SCC, squamous cell cervical cancer; ADC, adenocarcinoma of the cervix; ANOVA, analysis of variance.

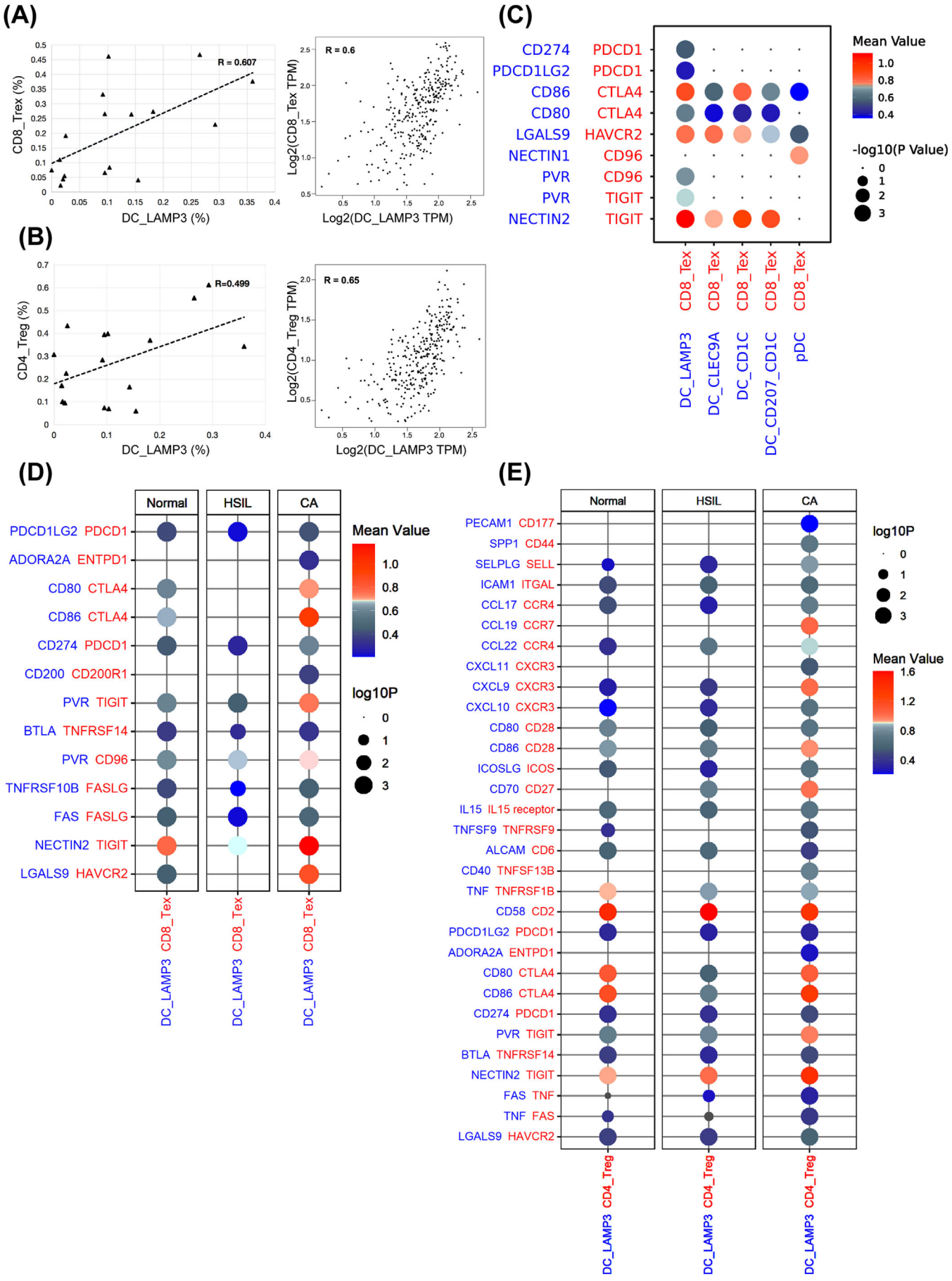
(A)
CD8_Trex (%)
DC_LAMP3 (%)
R = 0.607
Log2(CD8_Tex TPM)
Log2(DC_LAMP3 TPM)
R = 0.6
(B)
CD4_Treg (%)
DC_LAMP3 (%)
R=0.499
Log2(CD4_Treg TPM)
Log2(DC_LAMP3 TPM)
R = 0.65
(C)
CD274 PDCD1
PDCD1LG2 PDCD1
CD86 CTLA4
CD80 CTLA4
LGALS9 HAVCR2
NECTIN1 CD96
PVR CD96
PVR TIGIT
NECTIN2 TIGIT
CD8_Tex
DC_LAMP3
DC_CLEC9A
DC_CD1C
DC_CD207_CD1C
pDC
Mean Value
-log10(P Value)
(D)
Normal
HSIL
CA
PDCD1LG2 PDCD1
ADORA2A ENTPD1
CD80 CTLA4
CD86 CTLA4
CD274 PDCD1
CD200 CD200R1
PVR TIGIT
BTLA TNFRSF14
PVR CD96
TNFRSF10B FASLG
FAS FASLG
NECTIN2 TIGIT
LGALS9 HAVCR2
DC_LAMP3 CD8_Tex
Mean Value
log10P
(E)
Normal
HSIL
CA
PECAM1 CD177
SPP1 CD44
SELPLG SELL
ICAM1 ITGAL
CCL17 CCR4
CCL19 CCR7
CCL22 CCR4
CXCL11 CXCR3
CXCL9 CXCR3
CXCL10 CXCR3
CD80 CD28
CD86 CD28
ICOSLG ICOS
CD70 CD27
IL15 IL15 receptor
TNFSF9 TNFRSF9
ALCAM CD6
CD40 TNFSF13B
TNF TNFRSF1B
CD58 CD2
PDCD1LG2 PDCD1
ADORA2A ENTPD1
CD80 CTLA4
CD86 CTLA4
CD274 PDCD1
PVR TIGIT
BTLA TNFRSF14
NECTIN2 TIGIT
FAS TNF
TNF FAS
LGALS9 HAVCR2
DC_LAMP3 CD4_Treg
log10P
Mean Value

exhaustion. These findings verify the immunoregulatory role of the DC_LAMP3-CD8_Tex interaction, which potentially contributes to CC progression.

In terms of the cellular interplay between DC_LAMP3 cells and CD4_Tregs (Figure 5E), LAMP3_DCs produced multiple chemokines to attract and recruit CD4_Tregs, which were the most apparent in the CC group (CCL19-CCR7, CCL22-CCR4, and CXCL9/CXCL10-CXCR3). In addition, we observed closer adhesion-related interactions (SPP1-CD44 and ICAM1-ITGAL) in CC tissues than in normal cervical tissues and HSIL foci. Furthermore, we observed the activation of CD4_Tregs upon co-stimulation with DC_LAMP3 cells in the CC TIME. In particular, the costimulatory signals of activating CD4_Tregs (CD80/CD86-CD28, ICOSLG-ICOS) remained at a relatively low level in normal cervical tissues, indicating immune discrimination and tolerance from normal tissues. The signals were even lower within the HSIL foci, implying inactivation of CD4_Tregs and an efficient T-helper immune response targeting neoplastic cells; however, they reached the highest level in CC tissues (CD80/CD86-CD28, ICOSLG-ICOS, and CD70-CD27), indicating extensive activation of CD4_Tregs. Furthermore, we observed remarkable interactions related to immune escape (CD86-CTLA4, PVR/NECTIN2-TIGIT, and LGALS9-HAVCR2) in the CC group, which enhanced the immunosuppressive roles of CD4_Tregs and impaired the antitumor effects of other effector T cells. These results demonstrated that DC_LAMP3 cells interact with both neoantigen-reactive CD8_Tex cells and CD4_Tregs, thus synergistically mediating CC immune escape.

3.6 | IDO1 inhibition further enhanced the treatment efficacy of ICB in CC animal model

To further validate the association and interaction between DC_LAMP3 cells and neoantigen-reactive T cells in CC, including CD8_Tex and CD4_Treg cells, we performed multicolor IHC staining, which confirmed the physical co-localization of neoantigen-reactive T cells ($CD3^+$, $CD4^+/CD8^+$, and PD-1^+) and DC_LAMP3 cells ($CD80^+$ and PD-$L1^+$) evident in CC microenvironment compared with normal cervix and precancerous lesions (Figure 6A-B, Supplementary Figure S4).

As previously illustrated, we found that DC_LAMP3 cells specifically express IDO1 and actively participate in tryptophan metabolism, and DC_LAMP3 cells communicate with neoantigen-reactive T cells, including CD8_Tex cells and CD4_Tregs, which contribute to CC immune suppression and disease progression. On the basis of these findings, we hypothesized that the interaction between DC_LAMP3 cells and reactive T cells remodels the immunosuppressive environment in CC and that IDO1 may greatly contribute to this process. Furthermore, we hypothesized that the combination of an IDO1 inhibitor and ICB might benefit patients with CC. To test this hypothesis, we constructed a subcutaneous tumorigenesis model in C57BL/6 mice using murine CC cells (TC1) to evaluate the effectiveness of combined therapy with an IDO1 inhibitor (epacadostat, E) and ICB (Figure 7A-B). Compared with the untreated group, the anti-PD-1, anti-CTLA4, and anti-TIGIT groups exhibited reduced tumor growth. Although the independent use of the IDO1 inhibitor did not reduce tumor growth, combined treatment with the IDO1 inhibitor and ICB (anti-PD-1, anti-CTLA4, and anti-TIGIT agents) decreased the enzymatic activity of IDO1 and tended to cause a greater reduction in both tumor volume and weight than the administration of an ICB agent alone. This result was particularly observed in the anti-CTLA4 + E group, in which this difference was statistically significant (Figure 7C-D, Supplementary Figure S5A-D), suggesting that combination therapy could effectively inhibit CC inhibition in vivo. In addition, we investigated $CD8^+$ T cell infiltration and the immune response after treatment with IDO1 inhibitor and/or ICB. Although $CD8^+$ T cell abundance did not

FIGURE 5 DC_LAMP3 cells communicate with both reactive CD8_Tex cells and CD4_Tregs. (A) Scatter plot indicating the positive association between the abundance of CD8_Tex cells and that of DC_LAMP3 cells in the cervical environment, according to the present study (left panel, Pearson's correlation, R = 0.607) and TCGA CESC dataset (right panel, Pearson's correlation, R = 0.6, *P* value < 0.0001). (B) Scatter plot indicating the positive association between the abundance of CD4_Tregs and that of DC_LAMP3 cells in the cervical environment, according to the present study (left panel, Pearson's correlation, R = 0.499) and TCGA CESC dataset (right panel, Pearson's correlation, R = 0.65, *P* value < 0.0001). (C) Dot plot demonstrating selected ligand-receptor interactions between different DC groups and CD8_Tex cells. The involved cell types and ligand-receptor interactions are indicated by the columns and rows, respectively. The means of the average expression levels of two interacting molecules are indicated by the color gradation, with blue to red representing low to high expression, respectively. The "-Log10(*P* values)" are indicated by dot size. (D-E) Dot plots demonstrate selected ligand-receptor interactions between DC_LAMP3 cells and CD8_Tex cells (D), as well as those between DC_LAMP3 cells and CD4_Tregs (E) in the normal cervix, HSIL, and CA (cancer) groups. The histologic subtypes and ligand-receptor interactions are indicated by the columns and rows, respectively. The means of the average expression levels of two interacting molecules are indicated by the color gradation, with blue to red representing low to high expression, respectively. The "-Log10(*P* values)" are indicated by dot size. Abbreviations: TCGA, The Cancer Genome Atlas; CESC, cervical and endocervical cancer.

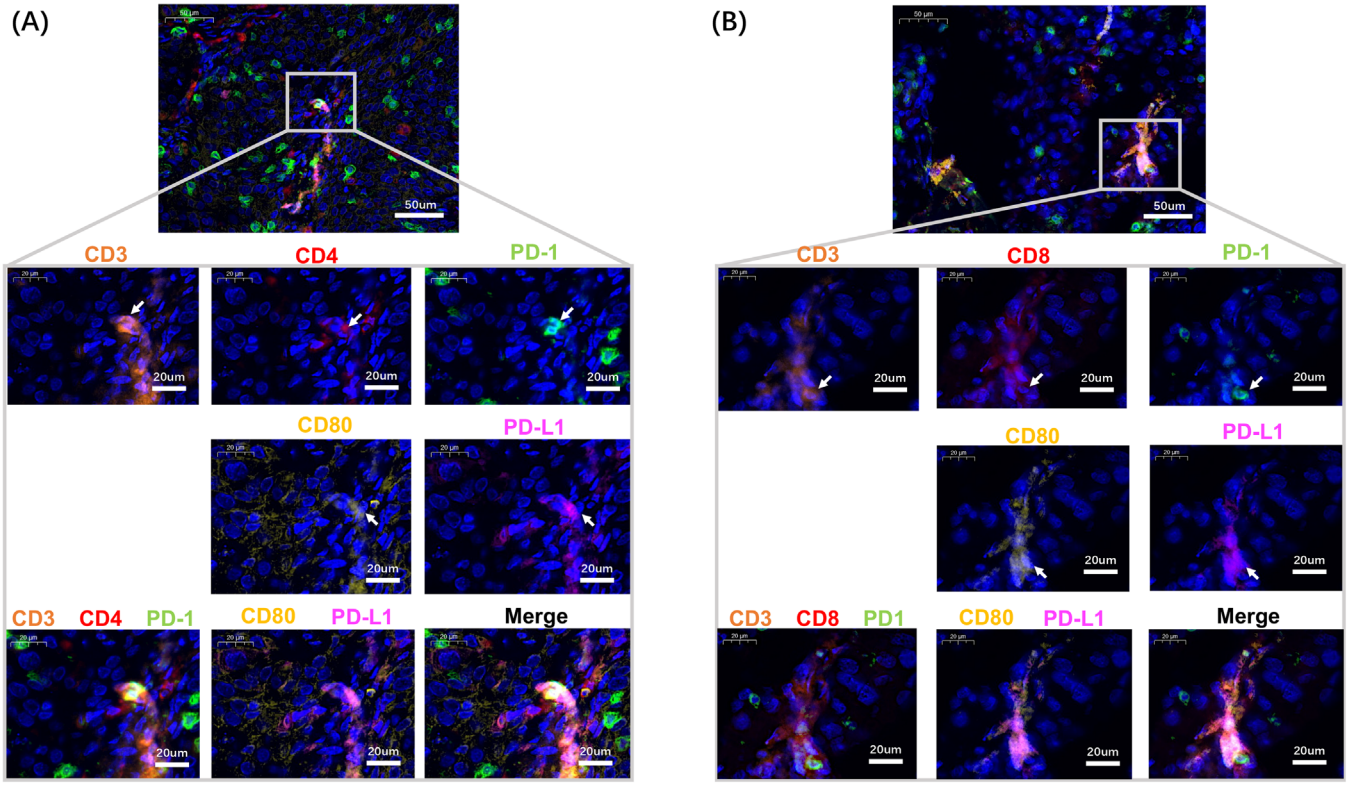

FIGURE 6 Co-localization of reactive T cells and DC_LAMP3 cells in CC TIME. (A) Representative images of multiplex IHC staining for the co-localization of Treg cells ($CD3^+CD4^+PD\text{-}1^+$) and DC_LAMP3 cells ($CD80^+PD\text{-}L1^+$) in CC tissue samples. Proteins that were detected using the respective antibodies are indicated on the top. The orange, red, green, yellow, and magenta arrows indicate cells in CC tissue samples with positive expression of the CD3, CD4, PD-1, CD80, and PD-L1 proteins, respectively (bottom panel). Scale bars, 50 μm and 20 μm for the top and bottom panels, respectively. (B) Representative images of multiplex IHC staining for the co-localization of CD8_Tex cells ($CD3^+CD8^+PD\text{-}1^+$) and DC_ LAMP3 cells ($CD80^+PD\text{-}L1^+$) in CC tissue samples. Proteins that were detected using the respective antibodies are indicated on top. The orange, red, green, yellow, and magenta arrows indicate cells in CC tissue samples with positive expression of the CD3, CD8, PD-1, CD80, and PD-L1 proteins, respectively (bottom panel). Scale bars, 50 μm and 20 μm for the top and bottom panels, respectively. Abbreviations: DCs, dendritic cells; CC, cervical cancer; TIME, tumor immune microenvironment; Treg, regulatory T cells; Tex, exhausted T cells; IHC, immunohistochemistry.

significantly differ between the groups (Figure 7E), the following characteristics were significantly different in the ICB + E groups, especially in the anti-PD-1 + E group, compared with the control group/E group/anti-PD-1 group: proliferation, represented by Ki67 expression; cytotoxicity, represented by GZMB expression; and immune reaction, represented by TNF-a expression (Figure 7F-H). Additionally, CXCL13 expression, which indicates tumor antigen reactivity, was higher after the application of ICB + E than after the application of an ICB agent alone; however, the difference was not statistically significant (Figure 7I). Collectively, these findings demonstrate that IDO1 inhibition further enhances the treatment efficacy of ICB by stimulating $CD8^+$ T-cell proliferation and effector function, providing essential clues for the development of combined immune therapy for CC.

4 | DISCUSSION

In the present study, against our expectations, malignant cervical epithelial cells did not show noticeable signs of tumor escape. Therefore, we focused our attention on immune cells, especially DCs, which are responsible for antigen processing and presentation, as well as T cells, which are indispensable components of the adaptive immune system and critical effectors of the antitumor response (Figure 8).

Current efforts to enhance the efficacy of immunotherapy have focused on reversing T-cell exhaustion and restoring antitumor functions, such as using anti-PD-1/anti-CTLA4 therapies targeting $CD8^+$ T cells or anti-PDL1 therapies targeting tumor cells [31]. However, less attention has been paid to other cell subsets in the TME

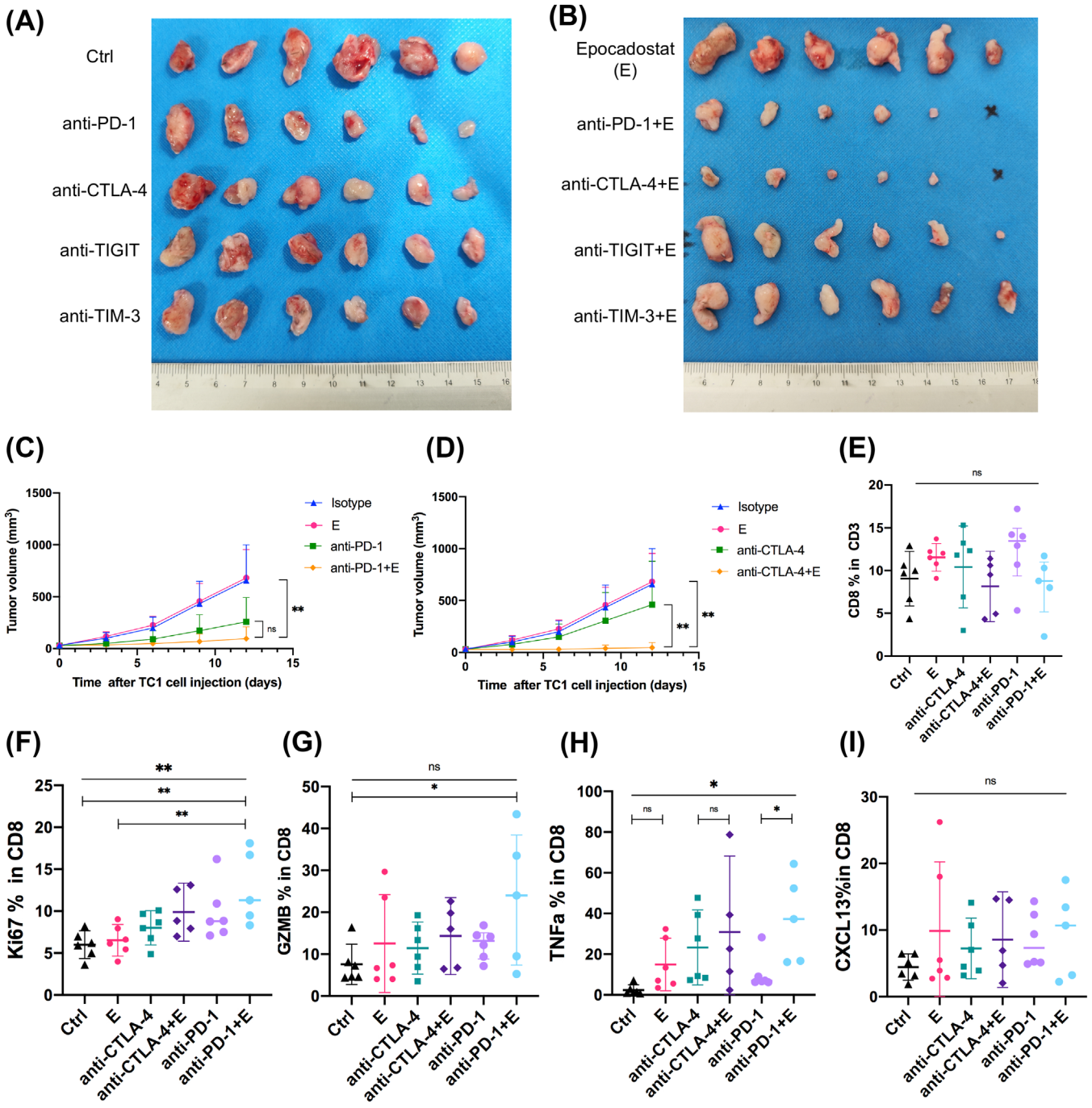

FIGURE 7 IDO1 inhibition further enhanced the treatment efficacy of ICB in CC animal models. (A-B) Photographs of TC1 tumors by indicated treatment. The tumors were removed from C57BL/6 mice on Day 12 after TC1 cell injection ($n = 6$ for each group in A: isotype as control group [Ctrl] and anti-PD-1, anti-CTLA4, anti-TIGIT, and anti-TIM3 groups; $n = 6$ for each group in B: Epacadostat [E], anti-PD-1 + E, anti-CTLA4 + E, anti-TIGIT + E, and anti-TIM3 + E groups). (C-D) Average tumor growth curves of TC1 tumors in mice that underwent different treatments. Error bar: mean ± SD ($n = 6$ for each treatment group). *P* values were obtained by one-way ANOVA with Tukey's multiple comparison test. *, $P < 0.05$; **, $P < 0.01$; ns, not significant. (E) Scatter plot showing CD8 expression in $CD3^+$ T cells from the peripheral blood of C57BL/6 mice bearing TC1 tumors after different treatment regimens through flow cytometry. Error bar: mean value with 95%CI ($n = 6$ for each treatment group). *P* values were obtained by one-way ANOVA. ns, not significant. (F-I) Scatter plots showing the expression of Ki67, GZMB, TNF-a, and CXCL13 in $CD8^+$ T cells from the peripheral blood of C57BL/6 mice bearing TC1 tumors after different treatment regimens through flow cytometry. Error bar: mean value with 95%CI ($n = 6$ for each treatment group). *P* values were obtained by one-way ANOVA with Tukey's multiple comparison test. *, $P < 0.05$; **, $P < 0.01$; ns, not significant. Abbreviations: IHC, immunohistochemistry; SD, standard deviation; ANOVA, analysis of variance.

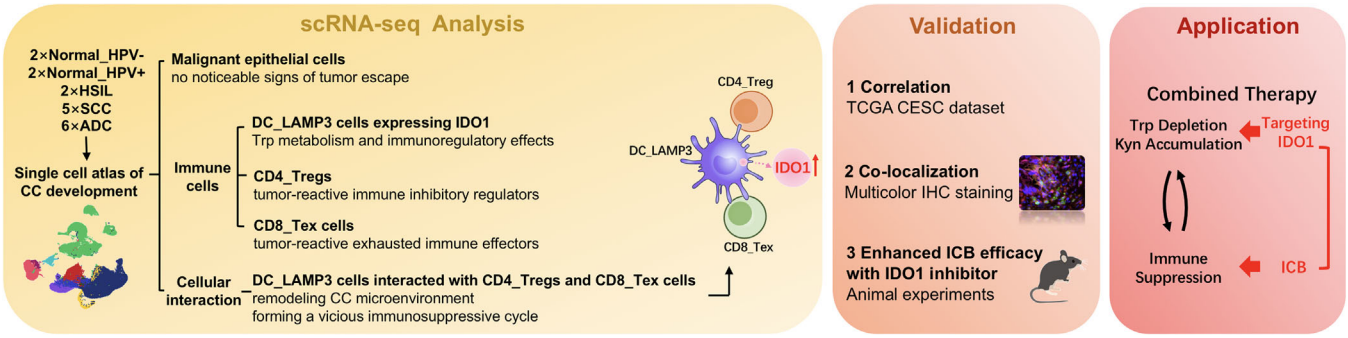

FIGURE 8 Flow chart and critical conclusions of the current study. Abbreviations: scRNA-seq, single cell RNA sequencing; HSIL, high-grade squamous intraepithelial lesion; SCC, squamous cell carcinoma; ADC, adenocarcinoma of cervix; CC, cervical cancer; DC, dendritic cells; Trp, tryptophan; Trp, tryptophan; Treg, regulatory T cells; Tex, exhausted T cells; TCGA, The Cancer Genome Atlas; CESC, cervical and endocervical cancer; IHC, immunohistochemistry; Kyn, kynurenine; ICB, immune checkpoint blockade.

that may also mediate malignant transition and immune suppression. DCs are a diverse group of specialized APCs that can promote immunity or tolerance by sampling and presenting antigens to T cells and by providing immunomodulatory signals through cell-cell contacts and cytokines in the context of cancer. Hence, we thoroughly investigated the DCs within the microenvironments of CC and precancerous lesions. DC_LAMP3 cells, characterized by specific LAMP3 and CD274 expression, showed a greater abundance in the CC ecosystem than in the non-cancer microenvironment and manifested a mature state and exerted immunoregulatory effects. These cells could be considered tolerogenic DCs in the context of CC, consistent with previous studies on other cancers [10, 32]. In addition, we observed that DC_LAMP3 cells promoted tryptophan metabolism by highly expressing IDO1, which encodes an enzyme that catalyzes the initial oxidation of L-tryptophan (L-Trp) and induces the accumulation of kynurenine (Kyn) metabolites. These metabolites have been reported to not only inhibit the proliferation and activity of $CD8^+$ T effector cells but also contribute to the differentiation of $CD4^+$ Treg cells, thus leading to immune dysregulation. These results further confirmed the tolerogenic and regulatory roles of DC_LAMP3 cells. In addition, we observed impaired tumor-associated antigen recognition and pro-angiogenic effects in DC_LAMP3 cells by analyzing the crosstalk between DC_LAMP3 cells and malignant epithelial cells. Collectively, these results indicate that DC_LAMP3 cells are a ubiquitous tolerogenic DC population in the CC TIME that regulate tryptophan metabolism and exhibit immune-regulatory functions, thus contributing to tumor escape and disease progression.

Additionally, our study revealed that DC_LAMP3 cells interacted with both neoantigen-reactive CD8_Tex cells and CD4_Tregs, thereby synergistically fostering an immunosuppressive niche in CC. We discovered that DC_LAMP3 cells not only attract, recruit, and activate CD4_Tregs through chemokines (CCL19-CCR7, CCL22-CCR4, and CXCL9/CXCL10-CXCR3) and costimulatory signals (CD80/CD86-CD28 and ICOSLG-ICOS) but also mediate CC immune escape through multiple immune checkpoint ligand-receptor pairs (CD274/PDL2-PDCD1, CD86-CTLA4, PVR/NECTIN2-TIGIT, and LGALS9-HAVCR2) between DC_LAMP3 cells and CD8_Tex/CD4_Treg cells. Some of these activities have been demonstrated in other cancers, highlighting the extensive importance of DC_LAMP3 cells during tumorigenesis. Intriguingly, the expression of IDO1 in DCs can be upregulated by immune checkpoint molecules on T cells, such as PD-1/CTLA4, further boosting tryptophan metabolism and forming a vicious immunosuppressive cycle [33, 34].

On the basis of these observations, we hypothesized that the combination of an IDO1 inhibitor and ICB could break this immunosuppressive cycle in CC by inhibiting tryptophan metabolism and restoring the antitumor function of T cells. Therefore, we established a subcutaneous tumorigenesis model in C57BL/6 mice with TC1 cells to assess the efficacy of combination treatment with an IDO1 inhibitor (epacadostat) and ICB (anti-PD-1, anti-CTLA4, anti-TIGIT, and anti-HAVCR2/TIM3 agents) in vivo. An anti-PD-1 agent plus epacadostat and an anti-CTLA4 agent plus epacadostat demonstrated better efficacy in inhibiting tumor growth than either ICB or epacadostat alone. Regarding the restoration of antitumor immunity, an anti-PD-1 agent plus epacadostat showed the best performance and enhanced $CD8^+$ T cell proliferation and cytotoxicity. In summary, we verified through animal experiments that IDO1 inhibition could further enhance the treatment efficacy of ICB drugs, especially anti-PD-1 agents, in CC by stimulating $CD8^+$ T-cell proliferation and effector function, offering critical clinical

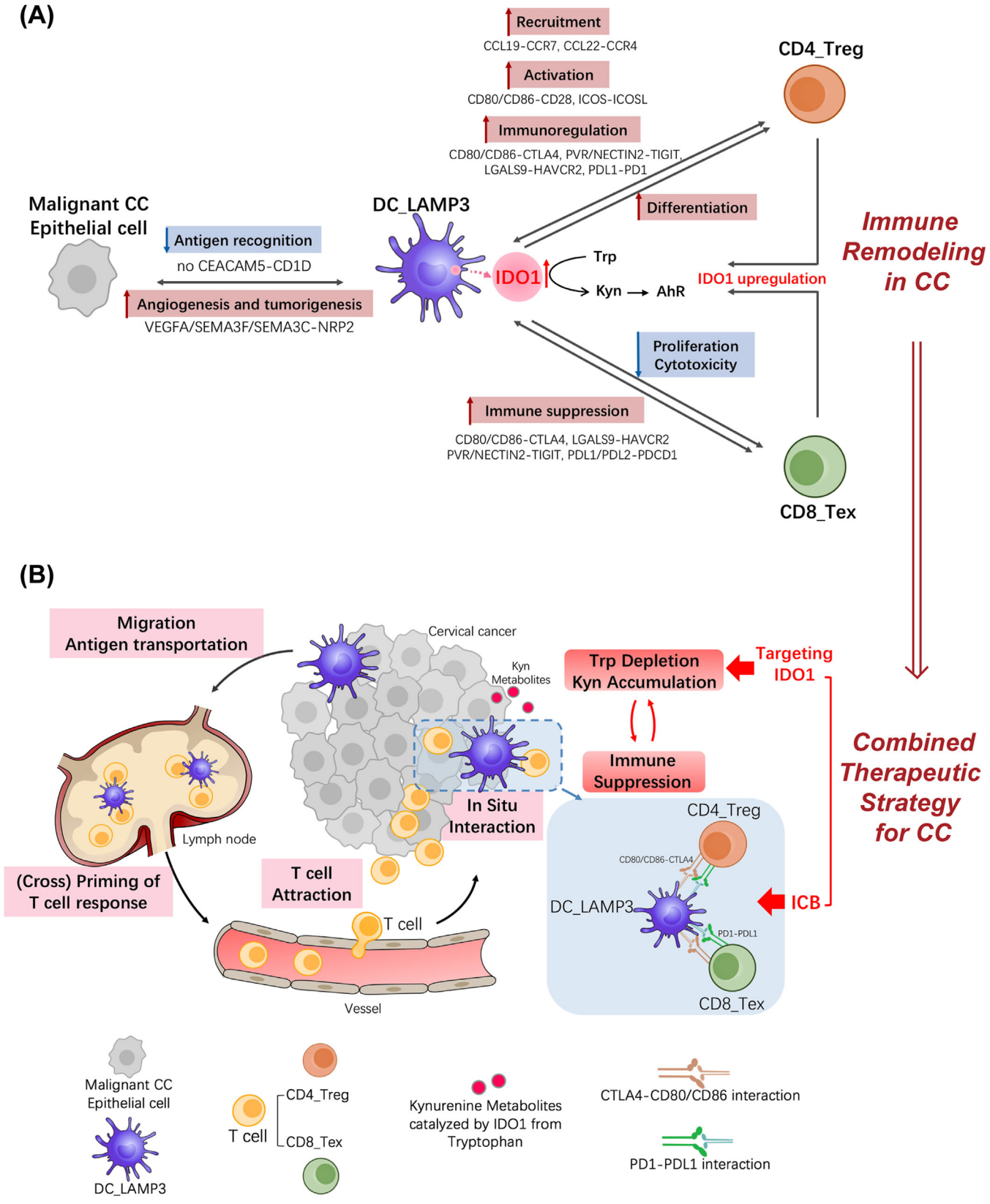

FIGURE 9 Schematic diagrams illustrating the vicious immunosuppressive cycle formed by DC_LAMP3 cells and reactive T cells in the CC TME and a potential therapeutic strategy. (A) From the perspective of tumor immunity, cellular crosstalk between DC_LAMP3 cells and malignant CC epithelial cells induces impaired antigen recognition and immune tolerance, whereas the interplay between DC_LAMP3 cells and CD4_Tregs and CD8_Tex cells is associated with recruitment, immunoregulation, and immunosuppression. From the perspective of tumor metabolism, the upregulation of IDO1 in DC_LAMP3 cells can convert Trp to Kyn metabolites, which activate AhR pathways and

insight. IDO1 is an attractive therapeutic target owing to its biological importance in cancer immunotherapy. Till date, several IDO1 inhibitors, including epacadostat [35], BMS986205 [36], and indoximod [37], have advanced into clinical trials. Although some studies have reported that IDO1 inhibitors combined with immune checkpoint inhibitors (pembrolizumab/nivolumab/ipilimumab) showed markedly enhanced antitumor efficacy in solid tumors [38, 39], negative results were reported in a phase III trial (NCT02752074) that investigated the efficacy and safety of a combination treatment with pembrolizumab and epacadostat in participants with unresectable and metastatic melanoma [40]. This led to the termination or withdrawal of other phase III trials, such as NCT03310567, NCT01685255, NCT03361228, NCT03463161, and NCT03325465, greatly hampering the development of IDO1 inhibitors. Considering that no clinical trials have yet been conducted to investigate the efficacy of IDO1 inhibitors combined with ICB for CC, we suggested that on the basis of our preclinical results, clinical trials should be considered and designed for patients with CC. Nevertheless, the following issues should be considered: (1) To achieve satisfactory IDO1-targeting therapy, insights into the structural features and inhibitory mechanisms of IDO1 should be prioritized. Novel therapeutic options targeting IDO1 could be introduced, including small-molecule inhibitors such as peptide vaccines and proteolysis-targeting chimeras (PROTAC) [41], which are emerging strategies for degrading oncogenic proteins via the ubiquitin-proteasome pathway. (2) Till date, a clear biomarker is lacking for PD-1/ PD-L1 therapy, since a combined positive score < 1 is only observed in approximately 10% of patients with CC, and even within this 10%, a minor response can be found where anti-PD-1/PD-L1 treatment is not indicated [42]. Therefore, we suggested that participant populations in clinical trials should be stratified according to IDO1 expression levels. Patients with CC presenting positive IDO1 expression may benefit more from combination therapy with an IDO1 inhibitor and ICB. In summary, we propose that the combination of IDO1 targeting with ICB could benefit patients with CC (Figure 9); however, rationally designed clinical trials and alternative IDO1-targeted therapies are urgently needed.

Nevertheless, our study has several limitations. First, neoantigen-reactive T cells were identified on the basis of only reported gene markers, without DNA levels, to evaluate tumor somatic mutations and neoantigens. Another major limitation of the conclusions of our data was the use of subcutaneous flank xenograft. The use of an orthotopic metastatic model transplanted into the cervical cavity region could provide more valuable insight into the ability of combined use of IDO1 inhibitor and ICB to inhibit the progression of CC. Additionally, a deeper mechanistic study is needed for investigating the pathway upstream of IDO1 upregulation in tolerogenic DC_LAMP3 cells to further reinforce our understanding of the CC immune landscape and illustrate the underlying metabolic mechanisms of immune suppression in CC.

5 | CONCLUSIONS

The present results revealed the dynamic nature of the immune microenvironment in the cervix during disease progression from normal cervical tissue to precancerous lesions and cancer by demonstrating the key roles of specific immune subpopulations, including DC_LAMP3, CD4_Treg, and CD8_Tex cells. Considering the scRNA-seq data, results of multicolor IHC analysis, and animal experiments, we proposed that the interaction between IDO1-expressing DC_LAMP3 cells and reactive T cells synergistically reshapes the immunosuppressive microenvironment in CC. This suggested that a combined treatment targeting IDO1 and ICB (such as anti-PD1/anti-CTLA4 agents) could improve the therapeutic efficacy of current immunotherapies for patients with CC presenting positive IDO1 expression. Our results offered novel insights and critical clues for designing and conducting future clinical trials in patients with CC.

DECLARATIONS

AUTHOR CONTRIBUTIONS

Conceptualization: Junjun Qiu and Xinyu Qu. Data analysis and interpretation: Xinyu Qu and Chenyan Guo. Experiment conduction: Yumeng Wang, Qian Jiang, Xinyu Qu, and Tingting Ren. Manuscript writing and editing:

subsequently promote the differentiation of $CD4^+$ cells into CD4_Tregs and inhibit the proliferation and cytotoxicity of $CD8^+$ T cells. Consequently, the accumulation of CD4_Tregs and CD8_T ex cells within the CC TME and high expression of immune checkpoints on CD4_Tregs and CD8_T ex cells can further enhance IDO1 expression in DC_LAMP3 cells, thus forming a vicious immunosuppressive cycle. (B) DC_LAMP3 cells experience migration, antigen presentation, T cell attraction and activation, and interaction with T cells in CC, highlighting excessive tryptophan metabolism and immune suppression. To break this vicious immunosuppressive cycle in the CC TME, we suggest the application of a combination treatment targeting IDO1 and blocking immune checkpoints such as PD-1 and CTLA4 to affect tumor metabolism and immunity. Abbreviations: CC, cervical cancer; TME, tumor microenvironment; Trp, tryptophan; Kyn, kynurenine; AHR, aryl hydrocarbon receptor.

Junjun Qiu, Xinyu Qu, and Keqin Hua. Visualization: Yumeng Wang and Xinyu Qu. Supervision: Junjun Qiu and Keqin Hua. All authors read and approved the final manuscript.

ACKNOWLEDGEMENTS

The authors thank Novel Bioinformatics Ltd. Co. for scientific discussions and bioinformatics analysis with their NovelBrain Cloud analytical platform (www.novelbrain.com).

CONFLICTS OF INTERESTS STATEMENT

The authors declare that they have no competing interests.

FUNDING INFORMATION

This study was supported by funding from Medical Innovation Research of Shanghai Science and Technology (21Y11906900 and 22Y3190050), Shanghai Hospital Development Center (SHDC2020CR1045B, SHDC2020CR6009, SHDC2020CR4087, and SHDC22021307), Shanghai Municipal Health Commission (202040498), National Natural Science Foundation of China (81971361 and 82173188), and Program for Zhuoxue of Fudan University (JIF157600).

ETHICS APPROVAL AND CONSENT TO PARTICIPATE

Animal experiments were approved by the Animal Science Center of Fudan University (202011012S). All procedures involving human participants in this study were approved by the Institutional Ethical Committee of Obstetrics and Gynecology Hospital of Fudan University (2020-22). All participants provided written informed consent.

CONSENT FOR PUBLICATION

Not applicable.

DATA AVAILABILITY STATEMENT

The data that support the findings of this study are available from the corresponding authors upon request. Gene Expression Omnibus accession numbers for the scRNA-seq and TCR-seq data reported in this study are GSE197461 and GSE208653, respectively. All computer codes used in this study are publicly available.

ORCID

Keqin Hua https://orcid.org/0000-0002-4546-5229
Junjun Qiu https://orcid.org/0000-0002-2063-2684

REFERENCES

1. Siegel RL, Miller KD, Fuchs HE, Jemal A. Cancer statistics, 2021. CA Cancer J Clin. 2021;71(1):7–33.
2. Chung HC, Ros W, Delord JP, Perets R, Italiano A, Shapira-Frommer R, et al. Efficacy and Safety of pembrolizumab in previously treated advanced cervical cancer: results from the Phase II KEYNOTE-158 study. J Clin Oncol. 2019;37(17):1470–78.
3. Naumann RW, Hollebecque A, Meyer T, Devlin MJ, Oaknin A, Kerger J, et al. Safety and Efficacy of Nivolumab Monotherapy in Recurrent or Metastatic Cervical, Vaginal, or Vulvar Carcinoma: Results From the Phase I/II CheckMate 358 Trial. J Clin Oncol. 2019;37(31):2825–34.
4. Santin AD, Deng W, Frumovitz M, Buza N, Bellone S, Huh W, et al. Phase II evaluation of nivolumab in the treatment of persistent or recurrent cervical cancer (NCT02257528/NRG-GY002). Gynecol Oncol. 2020;157(1):161–66.
5. O'Malley DM, Oaknin A, Monk BJ, Selle F, Rojas C, Gladieff L, et al. Phase II study of the safety and efficacy of the anti-PD-1 antibody balstilimab in patients with recurrent and/or metastatic cervical cancer. Gynecol Oncol. 2021;163(2):274–80.
6. Schreiber RD, Old LJ, Smyth MJ. Cancer immunoediting: integrating immunity's roles in cancer suppression and promotion. Science. 2011;331(6024):1565–70.
7. Zhou C, Wei W, Ma J, Yang Y, Liang L, Zhang Y, et al. Cancer-secreted exosomal miR-1468-5p promotes tumor immune escape via the immunosuppressive reprogramming of lymphatic vessels. Mol Ther. 2022;30(2):976–77.
8. Wang Y, He M, Zhang G, Cao K, Yang M, Zhang H, Liu H. The immune landscape during the tumorigenesis of cervical cancer. Cancer Med. 2021;10(7):2380–95.
9. Roider T, Seufert J, Uvarovskii A, Frauhammer F, Bordas M, Abedpour N, et al. Dissecting intratumour heterogeneity of nodal B-cell lymphomas at the transcriptional, genetic and drug-response levels. Nat Cell Biol. 2020;22(7):896–906.
10. Liu Y, He S, Wang XL, Peng W, Chen QY, Chi DM, et al. Tumour heterogeneity and intercellular networks of nasopharyngeal carcinoma at single cell resolution. Nat Commun. 2021;12(1):741.
11. Ho DW, Tsui YM, Chan LK, Sze KM, Zhang X, Cheu JW, et al. Single-cell RNA sequencing shows the immunosuppressive landscape and tumor heterogeneity of HBV-associated hepatocellular carcinoma. Nat Commun. 2021;12(1):3684.
12. Hanada KI, Zhao C, Gil-Hoyos R, Gartner JJ, Chow-Parmer C, Lowery FJ, et al. A phenotypic signature that identifies neoantigen-reactive T cells in fresh human lung cancers. Cancer Cell. 2022;40(5):479–93.e6.
13. Zheng C, Fass JN, Shih YP, Gunderson AJ, Sanjuan Silva N, Huang H, et al. Transcriptomic profiles of neoantigen-reactive T cells in human gastrointestinal cancers. Cancer Cell. 2022;40(4):410–23.e7.
14. Qiu J, Qu X, Wang Y, Guo C, Lv B, Jiang Q, et al. Single-Cell Landscape Highlights Heterogenous Microenvironment, Novel Immune Reaction Patterns, Potential Biomarkers and Unique Therapeutic Strategies of Cervical Squamous Carcinoma, Human Papillomavirus-Associated (HPVA) and Non-HPVA Adenocarcinoma. Adv Sci (Weinh). 2023;10(10):e2204951.
15. Guo C, Qu X, Tang X, Song Y, Wang J, Hua K, et al. Spatiotemporally deciphering the mysterious mechanism of persistent HPV-induced malignant transition and immune remodelling from HPV-infected normal cervix, precancer to cervical cancer:

Integrating single-cell RNA-sequencing and spatial transcriptome. Clin Transl Med. 2023;13(3):e1219.
16. Chen S, Zhou Y, Chen Y, Gu J. fastp: an ultra-fast all-in-one FASTQ preprocessor. Bioinformatics. 2018;34(17):i884-90.
17. Qiu X, Mao Q, Tang Y, Wang L, Chawla R, Pliner HA, et al. Reversed graph embedding resolves complex single-cell trajectories. Nat Methods. 2017;14(10):979–82.
18. Yaari G, Bolen CR, Thakar J, Kleinstein SH. Quantitative set analysis for gene expression: a method to quantify gene set differential expression including gene-gene correlations. Nucleic Acids Res. 2013;41(18):e170.
19. Vento-Tormo R, Efremova M, Botting RA, Turco MY, Vento-Tormo M, Meyer KB, et al. Single-cell reconstruction of the early maternal-fetal interface in humans. Nature. 2018;563(7731):347–53.
20. Tang Z, Li C, Kang B, Gao G, Li C, Zhang Z. GEPIA: a web server for cancer and normal gene expression profiling and interactive analyses. Nucleic Acids Res. 2017;45(W1):W98-w102.
21. Kim N, Kim HK, Lee K, Hong Y, Cho JH, Choi JW, et al. Single-cell RNA sequencing demonstrates the molecular and cellular reprogramming of metastatic lung adenocarcinoma. Nat Commun. 2020;11(1):2285.
22. Jhunjhunwala S, Hammer C, Delamarre L. Antigen presentation in cancer: insights into tumour immunogenicity and immune evasion. Nat Rev Cancer. 2021;21(5):298–312.
23. Whiteside TL. Immune suppression in cancer: effects on immune cells, mechanisms and future therapeutic intervention. Semin Cancer Biol. 2006;16(1):3–15.
24. Collin M, Bigley V. Human dendritic cell subsets: an update. Immunology. 2018;154(1):3–20.
25. Kraehenbuehl L, Weng CH, Eghbali S, Wolchok JD, Merghoub T. Enhancing immunotherapy in cancer by targeting emerging immunomodulatory pathways. Nat Rev Clin Oncol. 2022;19(1):37–50.
26. Platten M, Nollen EAA, Röhrig UF, Fallarino F, Opitz CA. Tryptophan metabolism as a common therapeutic target in cancer, neurodegeneration and beyond. Nat Rev Drug Discov. 2019;18(5):379–401.
27. Claesson-Welsh L, Welsh M. VEGFA and tumour angiogenesis. J Intern Med. 2013;273(2):114–27.
28. Potiron VA, Sharma G, Nasarre P, Clarhaut JA, Augustin HG, Gemmill RM, et al. Semaphorin SEMA3F affects multiple signaling pathways in lung cancer cells. Cancer Res. 2007;67(18):8708–15.
29. Islam R, Mishra J, Bodas S, Bhattacharya S, Batra SK, Dutta S, Datta K. Role of Neuropilin-2-mediated signaling axis in cancer progression and therapy resistance. Cancer Metastasis Rev. 2022;41(3):771–87.
30. Zhang L, Yu X, Zheng L, Zhang Y, Li Y, Fang Q, et al. Lineage tracking reveals dynamic relationships of T cells in colorectal cancer. Nature. 2018;564(7735):268–72.
31. Litchfield K, Reading JL, Puttick C, Thakkar K, Abbosh C, Bentham R, et al. Meta-analysis of tumor- and T cell-intrinsic mechanisms of sensitization to checkpoint inhibition. Cell. 2021;184(3):596–614.e14.
32. Zhang Q, He Y, Luo N, Patel SJ, Han Y, Gao R, et al. Landscape and Dynamics of Single Immune Cells in Hepatocellular Carcinoma. Cell. 2019;179(4):829–45.e20.
33. Zhai L, Ladomersky E, Lauing KL, Wu M, Genet M, Gritsina G, et al. Infiltrating T Cells Increase IDO1 Expression in Glioblastoma and Contribute to Decreased Patient Survival. Clin Cancer Res. 2017;23(21):6650–60.
34. Fallarino F, Grohmann U, Hwang KW, Orabona C, Vacca C, Bianchi R, et al. Modulation of tryptophan catabolism by regulatory T cells. Nat Immunol. 2003;4(12):1206–12.
35. Tang K, Wu YH, Song Y, Yu B. Indoleamine 2,3-dioxygenase 1 (IDO1) inhibitors in clinical trials for cancer immunotherapy. J Hematol Oncol. 2021;14(1):68.
36. Blocking IDO1 Helps Shrink Bladder, Cervical Tumors. Cancer Discov. 2018;8(1):OF3.
37. Kumar S, Jaipuri FA, Waldo JP, Potturi H, Marcinowicz A, Adams J, et al. Discovery of indoximod prodrugs and characterization of clinical candidate NLG802. Eur J Med Chem. 2020;198:112373.
38. Gibney GT, Hamid O, Lutzky J, Olszanski AJ, Mitchell TC, Gajewski TF, et al. Phase 1/2 study of epacadostat in combination with ipilimumab in patients with unresectable or metastatic melanoma. J Immunother Cancer. 2019;7(1):80.
39. Jung KH, LoRusso P, Burris H, Gordon M, Bang YJ, Hellmann MD, et al. Phase I Study of the Indoleamine 2,3-Dioxygenase 1 (IDO1) Inhibitor Navoximod (GDC-0919) Administered with PD-L1 Inhibitor (Atezolizumab) in Advanced Solid Tumors. Clin Cancer Res. 2019;25(11):3220–28.
40. Long GV, Dummer R, Hamid O, Gajewski TF, Caglevic C, Dalle S, et al. Epacadostat plus pembrolizumab versus placebo plus pembrolizumab in patients with unresectable or metastatic melanoma (ECHO-301/KEYNOTE-252): a phase 3, randomised, double-blind study. Lancet Oncol. 2019;20(8):1083–97.
41. Hu B, Zhou Y, Sun D, Yang Y, Liu Y, Li X, et al. PROTACs: New method to degrade transcription regulating proteins. Eur J Med Chem. 2020;207:112698.
42. An J, Tang J, Li BX, Xiong H, Qiu H, Luo L, et al. Efficacy and Safety of the Anti-PD-L1 mAb Socazolimab for Recurrent or Metastatic Cervical Cancer: a Phase I Dose-Escalation and Expansion Study. Clin Cancer Res. 2022;28(23):5098–106.

SUPPORTING INFORMATION

Additional supporting information can be found online in the Supporting Information section at the end of this article.

How to cite this article: Qu X, Wang Y, Jiang Q, Ren T, Guo C, Hua K, et al. Interactions of Indoleamine 2,3-dioxygenase-expressing LAMP3$^+$ dendritic cells with CD4$^+$ regulatory T cells and CD8$^+$ exhausted T cells: synergistically remodeling of the immunosuppressive microenvironment in cervical cancer and therapeutic implications. Cancer Commun. 2023;43:1207–1228. https://doi.org/10.1002/cac2.12486